

21 New phosphorite samples of the Ediacaran Doushantuo Formation (South China) contain
22 abundant AITs exhibiting diverse morphotypes, which may be distinguished from filamentous
23 microfossils and endolithic microborings with a suite of morphological criteria based on optical
24 microscopy and scanning electron microscopy (SEM). Black shales of the Baizhu section contains
25 abundant pyrite framboids whose size distributions reveal significant temporal variations of redox
26 conditions in shallow marine waters that probably promoted the formation of the Doushantuo
27 phosphorites.

28 AITs in the phosphorites are categorized into three types and further into five subtypes (I-a, I-b,
29 II-a, II-b, and III) based on their morphologies and observed or interpreted associations with
30 various kinds of terminal pyrite crystals. Among these, subtype II-a, single striated microtubes
31 2-10 μm wide, are interpreted to have resulted from migration of intact pyrite framboids. Those of
32 subtype II-b, dense clusters of outward radiating microtubes with consistent widths and
33 inward-facing cusped ridges, likely have formed by explosive disintegration and propulsion of
34 pyrite framboids due to highly concentrated carbon dioxide gas during the oxidation of organic
35 matter. During early diagenesis, formation of euhedral and framboidal pyrites involve a suite of
36 biogeochemical and physical processes including non-biological oxidation of organic matter and
37 reduction of sulfate in the presence of ferrous iron. Following the burial of pyrites, further
38 oxidative degradation of organic matter produced abundant CO_2 gas, which drives the pyrites to
39 move through the solid, but not yet fully lithified phosphatic gel composing granules. This model
40 explains the formation of previously reported but unexplained star-burst type AITs and it may be
41 tested by experimental studies.

42 Our new observations provide evidence for the widespread occurrence of AITs in the

43 Doushantuo phosphorites and urges careful petrographic examinations and differentiation between
44 AITs and morphologically similar biogenic microstructures.

45 Keywords: Phosphorite; Microtubes; Non-biological sulfate reduction; Oxidation of organic
46 matter; Paleoredox variations.

47 **1. Introduction**

48 Ambient Inclusion Trails (AITs) are a relatively rare but intriguing component of the rock
49 record, first reported as “ambient pyrites” from the Gunflint chert in North America (Tyler and
50 Barghoorn, 1963). They have been described in detail from a number of Precambrian successions,
51 including the 1.9-2.0 Ga Gunflint and Biwabik Formations on the southwestern margin of the
52 Superior Craton (Tyler and Barghoorn, 1963), the 3.5 Ga Warrawoona Group (Awramik et al.,
53 1983), the c. 3.4 Ga Strelley Pool Formation (Wacey et al., 2008a) and the 2.7 Ga Fortescue
54 Group (Knoll and Barghoorn, 1974; Lepot et al., 2009; Lepot et al., 2011) of Western Australia ,
55 and the Ediacaran Doushantuo Formation in South China (Zhang, 1984; Xiao and Knoll, 1999).
56 In thin section, AITs appear as void or infilled microtubes that terminate in a metal-rich grain
57 (typically pyrite), which is of equivalent diameter to the tubular trail itself.

58 AITs have been studied for the genesis of their unique morphology. As the width of the
59 microtubes systematically conforms to the diameter of the terminal pyrite crystals, it is apparent
60 that the pyrites had moved through the precursor microcrystalline chert matrix, leaving mineral
61 trails in their wakes(Wacey et al., 2008b). The driving mechanism of the pyrite, however, remains
62 unclear. It is generally hypothesized that the heating decomposition of organic matter attached to
63 the pyrites is necessary for the formation of AITs(Wacey et al., 2008b). Previous reports have been

64 mainly focused on siliceous rocks, so it is uncertain whether the proposed genetic mechanisms for
65 AITs in chert is applicable to AITs in other types of rock, such as phosphorites. A few studies have
66 reported AITs from phosphorites of the Doushantuo Formation (Xiao and Knoll, 1999; Liu and
67 Yin, 2006), but a thorough study of their mineral structure and a detailed petrographic
68 documentation has yet to be presented to explain their formation. In addition, relatively little
69 attention has been paid to the terminal grains of AITs in previous studies.

70 In this work, we observed abundant AITs and pyrite framboids from the Doushantuo
71 Formation in the Baizhu phosphorus mine near Baokang City, north Yangtze Block. For
72 comparison, samples from phosphorite mines in Taopinghe, ca. 60 km south of Baizhu, and
73 Weng'an, southwest Yangtze Block were also studied. Detailed petrography by optical microscopy,
74 scanning electron microscopy (SEM) and micro-Raman spectroscopy are presented here to discuss
75 the origin of AITs and their associated pyrites, which can help to understand non-biological
76 processes involved in the decomposition of biomass and to reconstruct the oceanic redox
77 conditions of the Doushantuo basins.

78 **2. Geological setting and samples**

79 The Doushantuo Formation is a carbonate-black shale-phosphorite sequence and now appears
80 as a lithostratigraphic zone distribution on the Yangtze Block (Jiang et al., 2011). It is underlain by
81 Cryogenian glacial and interglacial successions, and is overlain by carbonates of the Dengying
82 Formation. The depositional age of the Doushantuo Formation is constrained by many
83 geochronological studies. A zircon U-Pb age of 636.4 ± 4.9 Ma from the Cryogenian Nantuo
84 tillites constrains the maximum age of the Doushantuo Formation (Zhang et al., 2008). Zircon

85 U-Pb TIMS age data from ash beds have been published from the Yangtze Gorges area, including
86 635.26 ± 1.07 Ma, 632.48 ± 1.02 Ma and 651.09 ± 1.02 Ma ages from Members I, II and IV of the
87 Doushantuo Formation (Condon et al., 2005). Liu et al (2009) also reported a 614 ± 7.6 Ma zircon
88 U-Pb age from an ash bed in strata correlated to Member II. In addition, whole rock Re-Os
89 isochron ages of 598 ± 16 Ma (Kendall et al., 2009) and 591.1 ± 5.3 Ma (Zhu et al., 2013) from
90 member IV black shales have also been reported.

91 The Baizhu section is located in the north of the Yangtze Block (Fig. 1a). The samples studied
92 herein were collected from outcrops in the Baizhu mining area (GPS coordinates: $31^{\circ}40'52.9''\text{N}$,
93 $110^{\circ}56'20.1''\text{E}$) near Baokang City (Fig. 1a). The stratigraphy of this ~ 60 m thick studied section
94 is somewhat similar to that of the Jiulongwan section although a one-to-one correlation of the
95 classic four-member sequence is not evident (Fig. 1b). A ca. 2.5 m- thick basal cap dolostone is
96 observed, with abundant, partly-filled sheet cracks. Phosphorus-bearing horizons are interbedded
97 with dolostone and cherty shale (Fig. 1b). The main phosphorus-bearing horizon (horizon 12 in
98 Fig. 1b) consists of dolostone-phosphorite cycles containing cherty phosphatic lenses,
99 stromatolites, concretions and micro-oncoids. These rocks locally contain P_2O_5 up to 38 wt% (She
100 et al., unpublished data) and are actively mined in the study area. The presence of stromatolites,
101 micro-oncoids and abundant cyanobacterial fossils indicates that these phosphorites were formed
102 within the photic zone, and Zhou et al. (2004) proposed that they were deposited in a shallow
103 subtidal to intertidal, high energy environment, above the fair-weather wave base. Further
104 up-section, the sequence is characterized by medium-thickly bedded dolostones and cherty black
105 shales, which eventually grade upward into the thickly bedded dolostones of the Dengying
106 Formation. According to an earlier paleogeographic reconstruction by Jiang et al. (2011), both the

107 Baizhu and Taopinghe sections were deposited on the proximal margin of an intra-shelf basin.

108 Two granular phosphorite samples (*ZK511-30 and ZK511-32*) were collected from a drill hole
109 (GPS coordinates: 27°02'31"N, 107°24'15"E) in Weng'an phosphorus mine, southwest Yangtze
110 Block, corresponding to the "black bituminous phosphorite" of unit 4A of the Doushantuo
111 Formation described in Xiao et al. (2014). Location and geological settings of an additional
112 granular phosphorite specimen (*TP0901*) from the Taopinghe phosphorus mine (GPS coordinates:
113 31°16'29.9"N, 111°16'30.8"E), ~65 km north of Yichang are described in She et al. (2013).

114 **3. Methods**

115 3.1. Optical microscopy

116 Petrographic studies were performed on polished thin sections with a Nikon LV100 POL or a
117 Zeiss Axio Scope. Diameters of 1876 pyrite framboids in nine thin sections were measured under
118 reflected light along several parallel lines across each thin section until a size population of more
119 than 190 framboids was achieved.

120 3.2. Micro-Raman spectroscopy

121 Micro-Raman spectroscopic imaging was performed at the London Centre for Nanotechnology
122 with a WITec alpha 300R system equipped with a 532 nm laser with output power maintained at
123 ~5 mW. Raman hyperspectral scans were performed with a 100X objective (N.A. = 0.9) and a
124 50µm diameter optic fiber, and collected on a Peltier-cooled EMCCD detector for acquisition
125 times between 0.4 and 0.6 seconds per spectrum. Spatial resolution was ~360 nm/pixel and

126 spectral resolution was $\sim 4 \text{ cm}^{-1}$. Raman hyperspectral analyses were performed ≥ 1 micron below
127 the thin section surface, therefore ruling out potential artifacts induced by polishing or surface
128 contamination. Raman spectral images of mineral associations were generated by mapping peak
129 intensity for specific chemical bonds in minerals from each spectral scan using the WiTec Project
130 software (Bernard et al., 2008; Papineau et al., 2010).

131 Spot analysis by micro-Raman spectroscopy was also conducted at the State Key Laboratory
132 of Geological Processes and Mineral Resources, China University of Geosciences (Wuhan), with a
133 Thermo Scientific DXR dispersive Raman micro-spectrometer equipped with a petrographic
134 microscope (Olympus BX51) and a 532 nm Nd-YVO₄ laser. The output laser power was
135 maintained at ~ 10 mW. The use of a grating with 900 grooves per mm and a pinhole with 25 μm
136 diameter produced Raman spectra from 3500 to 50 cm^{-1} with a spectral resolution of $\sim 3 \text{ cm}^{-1}$.
137 Raman spectra were collected in 10 accumulations of 5 s each.

138 All measurements were conducted under conditions of atmosphere pressure, room temperature
139 ($21 \pm 1^\circ\text{C}$) and humidity $< 50\%$. Raman spectral characteristics of organic matter (OM) were
140 obtained after processing the data with a cosmic ray reduction routine and background subtraction
141 with a polynomial fit followed by peak deconvolution using a Lorentzian function.

142 3.3. Scanning electron microscopy

143 Scanning electron microscopy (SEM) was carried out at China University of Geosciences
144 (Wuhan). Images were acquired with both secondary electrons (SEI) and backscattered electrons
145 (BSE) with a FEG Quanta 200 environmental SEM or a Hitachi SU8010 field emission SEM, both
146 equipped with an energy dispersive X-ray spectrometer (EDS). Accelerating voltage was 2.5 kV

147 (FEG Quanta 200) or 15 kV (Hitachi SU8010) for SEI mode and 7.5 kV (FEG Quanta 200) or 15
148 kV (Hitachi SU8010) for BSE mode during imaging and analysis. Samples were coated with a
149 thin layer of gold or platinum prior to SEM analyses and after Raman analyses.

150 **4. Results**

151 4.1. Petrography

152 Four main types of phosphorite can be recognized in the Baizhu section based on their
153 sedimentary structures (Figs. 2a-d). Type 1 is banded phosphorite (Fig. 2a), which is characterized
154 by alternating layers of phosphate, dolomite and chert (Figs. 2e and g). The phosphatic layers
155 consist of organic-zoned granules (micro-oncoids, Fig. 2f) or generally ellipsoidal clots (Fig. 2h)
156 or granules that often contain AITs (Fig. 2i). Type 2 includes stromatolite-like and lenticular
157 phosphorites (Fig. 2b). Stromatolite-like structures can be non-branching columnar, or
158 dome-shaped and wavy. They are characterized by discontinuous organic-rich laminae 30-40 μm
159 in thickness (Fig. 2j). AITs occur in both the organic-rich laminae and the transparent groundmass,
160 but they are locally enriched in the transparent apatite groundmass (Fig. 2k). Type 3 consists of
161 concretionary phosphorite (Fig. 2c). Concretions are generally elliptical and variable in size, range
162 between major axes of 3 to 6 cm, and minor axes of 2 to 5 cm. They are typically brownish and
163 appear to be silicified and surrounded by a layer of dolomite. Type 4 is intraclastic phosphorite
164 (Fig. 2d), composed of abundant, medium-sand sized angular to subangular grains of detrital
165 quartz along with phosphatic and carbonate intraclasts and rhombs cemented by clear, isotropic
166 apatite. By contrast, samples from Weng'an and Yichang granular phosphorite all display a

167 granular texture (Fig. 2i), similar to those described in She et al. (2013).

168 According to previously published powder X-ray diffraction, infrared spectral and
169 geochemical data, the phosphate minerals in the Baizhu mining area are exclusively carbonate
170 fluorapatite (Huang, 1989).

171 4.2. Petrographic characteristics of the AITs

172 AITs are present in all the four types of phosphorites in Baizhu, with those in organic-rich
173 banded phosphorite and concretionary phosphorite displaying smaller diameters. In general, AITs
174 appear to preferentially occur in light-colored portions in banded or intraclastic phosphorite (Table
175 1). In the Doushantuo phosphorite in Yichang and Weng'an, however, they are often observed
176 from inside phosphatic granules (Figs. 2i and 3m-3u). Occasionally, extremely abundant AITs can
177 be observed in the isotropic, phosphatic groundmass of a type 1 banded phosphorite (Fig. 2l).

178 4.2.1 Morphology, size and distribution of the AITs

179 AITs have diverse morphologies (Figs. 2i, 2k-2l, 3a-3f, and 3m-3s), varying from straight, to
180 gently curved, to twisted and spiral forms. Occasionally, the path of a later AIT appears to have
181 been changed by collision with earlier terminal minerals (Fig. 3j). In some cases, the occurrence of
182 the Doushantuo AITs appears to be related to localized abundances of OM, despite the overall low
183 organic content of the host rock. As is shown in Figs. 3k and 3m-3n, the AITs radiate outwards
184 from an organic-rich central locus, similar to the star-burst type reported in Knoll and Barghoorn
185 (1974). This association might be diminished by later alteration during diagenesis and oxidative
186 weathering (Figs. 3d and 3e). In some specimens, pyrite crystals moved inward from the
187 outermost layer of phosphatic granules (Figs. 3p-3u). Occasionally, AITs can follow the outer

188 zones of phosphatic granules (Fig. 2i). Wherever AITs occur, the substrate is systematically
189 cryptocrystalline and isotropic under crossed nicols (Figs. 2l, 3a and 3q-3r).

190 The width of the AITs is variable (Table 1). In light-colored phosphorites, AITs are relatively
191 abundant, with diverse morphologies and variable diameters ranging from 2 to 68 μm . They are
192 often present in the interstitial cement containing pyrite aggregates that were later oxidized (Figs.
193 3d and 3e). The cross sections of AITs can be nearly circular (Fig. 3e), square (Figs. 4a and 4e),
194 sub-hexagonal (Fig. 4g) or irregular. In organic-rich banded phosphorites, AITs are less abundant
195 and are generally smaller, with width varying from 1 to 10 μm (Table 1).

196 4.2.2 Infilling material in the microtubes

197 AITs can be vacant (Figs. 3e and 4c-4d), partly filled (Fig. 4f), or completely filled (Figs. 4a
198 and 4e). In some cases, well-preserved casts of microtubes can be observed (Fig. 4e). The most
199 common infilling material is carbonate with diagnostic high-order white interference color (Table
200 1, Figs. 2l, 3a and 3q-3r), which is confirmed by Raman hyperspectral imaging (Figs. 3o and 3u).
201 The infillings in AITs are identified to be calcite with a strong Raman peak at 1092 cm^{-1} (weak
202 peaks at 157 cm^{-1} , 286 cm^{-1} , and 705 cm^{-1}) and sometimes, apatite with a strong Raman peak at
203 970 cm^{-1} (Fig. 6). Observations of thin sections stained with alizarin red S reagent further
204 document that most microtubes are filled with calcite. Other microtubes are coated with orange
205 Fe-oxide minerals that suggest oxidative weathering of sulfide (Figs. 3d and 3e).

206 4.2.3 Longitudinal striae

207 Longitudinal striae created by migration of terminal pyrite crystals are frequently observed on
208 the walls of the AITs (Figs. 3c, 3l and 4a-4d). Striae in AITs are diagnostically parallel and never
209 intersect with each other. In Figs. 4b-4d, inward-facing cusped longitudinal ridges (crude striae,

210 arrowed) are clearly visible, whereas in other AITs fine longitudinal striae with low relief are
211 present (Fig. 3a). Interestingly, the longitudinal ridges on the AIT casts in Fig. 4e correspond well
212 to the striae in Fig. 4a, although the crystal sizes of the casts are larger than the submicrometer
213 sized phosphatic groundmass. The striae are usually regularly spaced, with distances ranging from
214 0.3 to 1.9 μm (Table 2). In Fig. 4c, for instance, the spacing of longitudinal striae in a twisted AIT
215 measures around 0.7 μm .

216 4.2.4 Terminal grains

217 In some cases, terminal crystal grains can be observed at one end of the microtubes. These can
218 be a single pyrite crystal, which can be anhedral (Figs. 3c, 3g, and 3p-3q) or euhedral (Figs. 3i, 3k),
219 or a cluster of crystals (Fig. 3e). Some of the terminal pyrites retain their original crystal shape
220 (Figs. 3f and 3l), whereas others appear to have been modified (Fig. 3c).

221 4.3. Pyrite framboids and their possible association with AITs

222 In the Baizhu section, both individual euhedral to anhedral pyrite grains and pyrite framboids
223 are observed. Pyrite framboids generally occur in discontinuous black shale layers (horizons 8, 13,
224 14, 17, 20 and 23) which are separated by dolostone layers without framboids (horizons 9-12,
225 15-16, 18-19 and 21-22). Framboids range in size from 1 to 11 μm (Table 3) and are composed of
226 micro-crystals 0.4 to 1.5 μm across (Figs. 4h-4o, Table 2). The micro-crystals show
227 cubic-octahedron (Figs. 4h and 4i), pentagonal dodecahedron (Figs. 4j and 4k) and subspherical
228 (Fig. 4l) crystal forms. Framboids are often coated with a thin layer of amorphous (carbonaceous?)
229 material (Fig. 4m). In some cases, a thin (carbonaceous?) layer, or membrane covers each of the
230 micro-crystals (Fig. 4i). Within the dark sedimentary laminae, pyrite framboids are occasionally

231 aligned parallel (Fig. 4o). Pyrites hosted in dolostones and phosphorites can be oxidized during
232 post-depositional processes, as is shown in Fig. 3f where goethite is present as a pseudomorph
233 after pyrite. Pyrite aggregates with diameters between 35 and 80 μm can also be oxidized by
234 post-depositional fluid circulation in more porous areas (Figs. 3d and 3e).

235 The size distribution of pyrite framboids is shown in Table 3. In horizons 14 and 20, the
236 framboids are on average smaller and less variable, ranging in size between 2.9 and 3.3 μm (SD
237 between 0.9 and 1.3). Here the maximum framboid diameter (MFD) varies between 6.6 and 7.7
238 μm , and no framboid is larger than 10 μm . In horizons 8, 13, 17 and 23, the observed range of
239 mean framboid diameter is between 3.6 and 4.5 μm (SD between 1.0 and 1.7). Two populations
240 from horizon 17 contain relatively high proportions (16% to 29%) of framboids larger than 5 μm ,
241 with a MFD of 10.7 μm .

242 In the Doushantuo phosphorites, however, pyrite framboid is relatively rare and has hindered
243 direct comparisons between AITs and pyrite framboids. Examples of possible oxidized framboid
244 (Figs. 3g and h) and unambiguous pyrite framboid (Fig. 3i) have been observed from a
245 phosphorite sample in the Taopinghe section. The apparent diameter of the latter (5.8 μm) appears
246 to be slightly greater than the mean diameters of framboids in black shales but falls into the range
247 of the AIT widths.

248 Considering the rarity of well-preserved pyrite framboids in phosphorites, we tentatively
249 compared the sizes of framboids in black shales and AITs in phosphorites, which often occur in
250 adjacent layers at the scale of less than 1 cm. The SEM images of pyrite framboids show that most
251 micro-crystals are of similar size (Figs. 4h-4m). Ratios of overall framboid diameter to
252 micro-crystal diameter ($D_{\text{frm}}/d_{\text{frm}}$) range from 3.7 to 10.2. Interestingly, measurements of pyrite

253 frambooids and a group of smaller AITs yielded comparable results (Table 2). These AITs range in
254 width from 1.6 to 9.7 μm , whereas the spacings of longitudinal striae are 0.3 to 1.8 μm wide,
255 corresponding closely to the diameters of micro-crystals in the frambooids (0.4 to 1.5 μm). The
256 ratios of microtube diameter to longitudinal striation spacing ($D_{\text{AIT}}/d_{\text{AIT}}$) vary between 4.1 and 7.9
257 (Fig. 5), well within the range of dispersed $D_{\text{frm}}/d_{\text{frm}}$ ratios.

258 4.4. Raman spectroscopic characteristics and organic crystallinity

259 Micro-Raman spectroscopy has revealed the presence of carbonate, apatite and disseminated
260 OM in all the Doushantuo samples (Figs. 3o, 3u and 6). Major spectral peaks are systematically
261 detected at wavenumbers of 970 cm^{-1} , 1092 cm^{-1} , 1101 cm^{-1} , 1348 cm^{-1} and 1605 cm^{-1} (Fig. 6).
262 Apatite is characterized by the prominent peak at 970 cm^{-1} , whereas the other peaks (435 cm^{-1} ,
263 594 cm^{-1} , 1059 cm^{-1} and 2790 cm^{-1}) are weak due to the low degree of crystallinity of the
264 phosphate. The systematic presence of OM in the banded phosphorites is confirmed by the Raman
265 D- (1348 cm^{-1}) and G- (1600 cm^{-1}) bands. Interstitial cement between phosphatic granules is
266 dolomite with a strong peak at 1101 cm^{-1} (minor peaks at 181 cm^{-1} and 305 cm^{-1}). Although the
267 spectra of calcite and dolomite are similar, the systematic difference in their strong and weak peak
268 positions are resolvable (spectra 3-8 vs. 7 and 9 in Fig. 6).

269 The degree of graphitic order is indicated by Raman spectral parameters, which record peak
270 metamorphic conditions and remain unaffected by retrogression (Beyssac et al., 2002). As shown
271 in Fig. 6, the Raman spectra of OM in the Baizhu and Weng'an phosphorites are characterized by
272 the co-existence of D-band (indicating disordered OM) and G-band (graphitic OM) in the first
273 order region (1000 - 1800 cm^{-1}), which can be decomposed into five bands (G, D1, D2, D3, and

274 D4; Table 4). For the Baizhu samples, the D1-bands are centered between 1342 and 1350 cm^{-1}
275 (FWHM = 52 - 115 cm^{-1}) with a greater intensity, whereas the G-bands are centered at around
276 1600 cm^{-1} (FWHM = 41 - 45 cm^{-1}) and are of lower intensity (spectra 10 and 11 in Fig. 6, Table
277 4). In the Weng'an phosphorites, however, the G-band (1590 cm^{-1} , FWHM = 59 cm^{-1}) is more
278 prominent than the D1-band (1348 cm^{-1} , FWHM = 142 cm^{-1}) (spectra 12 and 13 in Fig. 6, Table
279 4). Using the empirical equations proposed by Lahfid et al. (2010), we calculated maximum
280 metamorphic temperatures of the OM in the Baizhu and Weng'an phosphorites to range between
281 290 and 360 °C except for sample BK10-8-2_02 (Table 4). This is similar to those estimated for
282 the Doushantuo phosphorites in Yichang (She et al., 2013). Notably, when compared with the
283 Baizhu samples, the Weng'an phosphorites appear to have formed under lower metamorphic
284 temperatures as indicated by their broader and lower D-bands (Kouketsu et al., 2014), which is
285 consistent with the lower calculated metamorphic temperature (sample ZK511-32_01 in Table 4).
286 These indicate a generally low degree of thermal maturation of the OM in these samples,
287 consistent with metamorphism at the prehnite-pumpellyite facies.

288 5. Discussion

289 5.1 Formation of pyrite framboids and their paleoredox implications

290 Pyrite formation involves complex processes that are controlled by the availability of
291 decomposable OM, dissolved sulfate, and reactive iron minerals (Berner, 1985). Nucleation and
292 growth of framboidal pyrites have been observed in euxinic conditions, such as the Black Sea
293 (Wilkin et al., 1997), and in anoxic sediment pore waters underlying oxygenated bottom waters,

294 such as the Great Salt Marsh, USA (Wilkin et al., 1996). Syngenetic framboids formed in euxinic
295 conditions are generally smaller and less variable in size than those formed diagenetically within
296 sediments underlying oxygenated waters, because the former have shorter residence times near the
297 oxic-anoxic boundary than the latter (Benning et al., 2000; Wilkin and Arthur, 2001). Both mean
298 and maximum diameters (MFD) of pyrite framboids have been used to discriminate between
299 euxinic and non-euxinic environments (Wilkin et al., 1996; Wilkin and Barnes, 1997; Wignall and
300 Newton, 1998; Nielsen and Shen, 2004). Bond and Wignall (2010) have also shown that the mean
301 size ranges of framboids forming in euxinic, anoxic and dysoxic environments are 3-5 μm , 4-6 μm
302 and 6-10 μm , respectively. The common occurrence of well preserved pyrite framboids in the
303 Doushantuo Formation attests to their potential as paleoredox indicators, although secondary
304 overgrowths of primary pyrites during burial diagenesis may obscure primary textures (e.g.,
305 Wacey et al., 2015) and result in a decrease in the proportion of framboidal pyrite (Benning et al.,
306 2000).

307 Pyrite framboid size distributions in the Baizhu section indicate the frequent occurrence of
308 euxinic, shallow marine conditions (Fig. 7). In horizons 14 and 20, the small mean diameter of
309 framboids (3.0 μm - 3.3 μm) and the absence of framboids larger than 10 μm suggest pyrite
310 formation within a euxinic water column. In horizons 8, 13, 17 and 23, the mean diameters of
311 framboids range between 3.6 and 4.0 μm . This, along with the abundance of small framboids with
312 diameters <5 μm , also indicate a euxinic environment. Among these, one sample from horizon 17
313 (BK17-2) shows a larger standard deviation (1.4 μm) and MFD (10.8 μm), and another sample
314 from horizon 17 (BK17-1) has a larger mean framboid diameter (4.5 μm) and standard deviation
315 (1.7 μm), with those >5 μm in diameter accounting for 29% of the total framboids. These two

316 samples indicate that a slightly higher redox state, probably transient development of dysoxic
317 condition, might have occurred in level 17.

318 Various proxies have been used previously to investigate the redox conditions of the
319 Doushantuo basins. Based on Fe speciation and S isotope data, Li et al. (2010) suggested that the
320 Ediacaran ocean was strongly stratified, with an oxic surface layer resting above a euxinic wedge
321 that was sandwiched within ferruginous waters on the continental shelf. Analyses of pyrite
322 framboids in the upper and lower slope sections of the Doushantuo Formation has revealed
323 decameter-scale euxinic and non-euxinic alternations (Wang et al., 2012). Guan et al. (2014) has
324 also shown the frequent redox fluctuations during the Ediacaran Period based on size distribution
325 and $\delta^{34}\text{S}$ of pyrite framboids, and redox sensitive element geochemistry of black shales in the
326 Ediacaran Lantian Formation in South China. A recent paleoredox study of late Ediacaran shales
327 in the Three Gorges area of South China has documented significant spatial redox heterogeneity
328 for the Doushantuo basins, even at the kilometer-scale (Li et al., 2015). All these models posit
329 oxygenated surface waters underlain by euxinic waters either below the chemocline or within the
330 deep bottom waters. It is somewhat surprising, therefore, that framboids indicative of euxinic
331 waters are observed in the shallow-water Baizhu section, which is considered to have been
332 deposited well above the chemocline that is defined in the coeval Jiulongwan and Xiaofenghe
333 sections (Li et al., 2010; Wang et al., 2012; Xiao et al., 2012; Cui et al., 2015). Moreover, it is
334 generally believed that marine sedimentary phosphate accumulation occurs above the oxygen
335 minimum zone (OMZ) and below the sediment water interface in both the Phanerozoic and
336 modern oceans (Slansky, 1986; Knudsen and Gunter, 2002). If, as it seems from our data,
337 framboidal pyrite in black shales from the Baizhu section records periods of water column euxinia,

338 it would appear that significant temporal redox fluctuations (Jiang et al., 2011; Wang et al., 2012)
339 or spatial redox heterogeneity (Li et al., 2015) existed during the Doushantuo Period. Fluctuations
340 of the chemocline led to the formation of the repeated cycles of black shale-phosphorite in the
341 Doushantuo Formation (She et al., 2014), followed by diagenetic formation of abundant AITs.
342 Although the cause of such redox variations remains unclear, euxinia might have developed
343 locally in shallow waters like the Baizhu basin, modulated by cyanobacterial blooms fueled by
344 continentally-derived nutrients (She et al., 2014) and increased sulfate availability following the
345 meltdown of the Snowball Earth as manifested by the underlying Nantuo tillites.

346 5.2 Criteria for the identification of AITs

347 Tyler and Barghoorn (1963) presented an initial description of AITs (which they called,
348 "ambient pyrites") from the Gunflint and Biwabik formations emphasizing that these inorganic
349 "pseudofossils" were not genetically related to the morphologically distinct microfossils occurring
350 in the same rocks. Knoll & Barghoorn (1974) proposed that AITs were formed by migration of
351 pyrite grains in the matrix driven by gas pressure produced by degradation of OM. However, such
352 structures have sometimes been alternatively interpreted as filamentous microfossils (Awramik et
353 al., 1983; Awramik, 1992; Baturin et al., 2000) or endolithic microborings (Dong et al., 1984;
354 Conway Morris and Bengtson, 1994; Zhang and Pratt, 2008) in subsequent publications. Xiao and
355 Knoll (1999) discussed the three hypotheses and favored the Knoll and Barghoorn interpretation
356 based upon the clearly visible longitudinal striae on the microtubes. McLoughlin et al. (2007) also
357 noted that longitudinal striae created by the facets of the propelled mineral grain would be absent
358 from endolithic microborings and are perpendicular to any annulations that might reflect cell

359 septation. Wacey et al. (2008b) reviewed previously published examples of AITs and proposed
360 nine criteria for the recognition of AITs by summarizing their morphological characteristics in
361 petrographic thin section. These include: (1) presence of a terminal mineral grain which is of
362 equivalent diameter to the microtubes; (2) presence of longitudinal striae along the wall of the
363 microtubes; (3) the cross section of the microtubes mirroring the crystal geometry of the terminal
364 grains; (4) unlike endolithic borings, AITs tend to occur both in the center and on the edge of a
365 grain; (5) AITs may radiate away from clumps of organic material; (6) AITs may become twisted
366 towards their ends; (7) they may display side branches showing a different diameter to the original
367 microtube; (8) the presence of sharp angular turns of the microtubes; (9) they may cross cut each
368 other and form tangled masses.

369 Here we propose two additional criteria for distinguishing AITs from filamentous microfossils.
370 The first is variability of size. AITs tend to occur in the rock matrix, and their diameters vary in a
371 single thin section from $< 10 \mu\text{m}$ to $> 50 \mu\text{m}$ (Figs. 2m and 3d). By contrast, filamentous
372 microfossils of the same taxon tend to have similar diameters. If there are more than one species
373 of filamentous microfossils, statistics of the size of filaments generally yield peaks with normal
374 distribution (e.g., Strother and Tobin, 1987; She et al., 2013), whereas sizes of AITs are not likely
375 to show similar distribution patterns. The second additional criterion concerns sharp outlines and
376 distinct infilling materials. AITs generally have sharp outlines if the microtubes are filled or coated
377 with minerals (e.g., calcite, Figs. 3a, 3d-3e, 3j, 3i, 3n-3p and 3r) that are different to the substrate
378 in refractory index, whereas filamentous fossils often show fuzzy outlines because the organisms
379 are embedded in cryptocrystalline silica or phosphate. Being one of the major products of the
380 non-biological oxidation of OM that lead to the formation of AITs (discussed below in detail), the

381 calcite infillings thus might serve as a criterion for the recognition of AITs. In the search for AITs
382 in phosphorites, as is shown in this study, examination of thin sections under crossed nicols is very
383 helpful because the high-order white interference color of the carbonate infillings are in sharp
384 contrast to the isotropic nature of the phosphatic groundmass.

385 With these criteria, it is possible to recognize many of these microtubular structures based on
386 petrographic observations. However, uncertainty remains in distinguishing AITs from similar
387 biological structures, especially endolithic microborings, and therefore further studies are needed.

388 5.3 Genesis of AITs

389 5.3.1 Terminal grains and other factors contributing to AIT formation

390 In the Baizhu, Taopinghe and Weng'an samples, terminal pyrite grains have been observed in
391 many AITs, such as aggregates of pyrite micro-crystals or single pyrite crystals, which are
392 sometimes oxidized or partly oxidized (Figs. 3c-f). In other cases, however, terminal grains were
393 not observed (Figs. 3a and 3h), mainly due to the limited thickness of the thin sections (ca. 30 μm).
394 These limitations hinder the establishment of the association of AITs and specific types of pyrites.

395 Another important feature of AITs is that longitudinal striae are often observed along the walls
396 of the microtubes. This provides critical evidence for the propulsion and migration of ambient
397 pyrite crystals (Knoll and Barghoorn, 1974; Xiao and Knoll, 1999; Wacey et al., 2008a; Lepot et
398 al., 2011). Precisely how such striae are generated, however remains elusive. Wacey et al. (2008b)
399 suggested that longitudinal striae are created by the facets of the propelled mineral crystal, but the
400 authors did not provide direct evidence. Others believe that they correspond to angular faces

401 formed in the wake of crystal movement (Lepot et al., 2011; Tiwari and Siddaiah, 2012). This
402 interpretation, however, do not explain the fact that the spacings between striae are much smaller
403 than the terminal pyrite crystals themselves in many of the observed AITs (Xiao and Knoll, 1999;
404 Wacey et al., 2008b). As shown in Table 2 and Fig. 5, diameters of pyrite framboids (D_{frm}) in
405 black shales are strikingly similar to those of the microtubes of AITs (D_{AIT}) in phosphorites.
406 Moreover, the sizes of the micro-crystals of framboids (d_{frm}) are in the same range as the spacing
407 of longitudinal striae (d_{AIT}), which yields similar $D_{\text{frm}}/d_{\text{frm}}$ and $D_{\text{AIT}}/d_{\text{AIT}}$ ratios. In addition, the
408 inward facing cusped ridges (crude longitudinal striae) on some of the AITs (Figs. 4b-d) appears
409 to reflect the surface morphology of framboids (e.g., Fig. 4i), whereas fine longitudinal striae (Fig.
410 4a) probably correspond to facets of single pyrite crystal. These suggest that at least some of the
411 AITs are probably caused by migration of pyrite framboids. The abundant occurrence of AITs in
412 the Doushantuo phosphorites implies that physical and chemical environments during
413 phosphatization probably facilitated the formation of pyrites and their subsequent propulsion and
414 migration through the phosphatic matrix.

415 Previous studies have shown that both sulfur oxidising bacteria (Froelich et al., 1988; Schulz
416 and Schulz, 2005; Bailey et al., 2007; Arning et al., 2009) and cyanobacteria (Papineau et al.,
417 2013; She et al., 2013; She et al., 2014; Papineau et al., 2016) might have played active roles in
418 the remineralization, recycling and precipitation of phosphorus. Extracellular polymeric
419 substances (EPS) produced by cyanobacteria, in particular, might have contributed to the final
420 precipitation of calcium phosphate (She et al., 2013). A close association between pyrite framboids
421 and biofilms has also been documented, although substantial debate remains on the extent to
422 which biology directly or indirectly contributes to framboid formation (Wacey et al., 2015).

423 Likewise, EPS may have also promoted the formation of AITs, in providing OM as a reactant for
424 AIT formation.

425 The decomposition of OM is also an important factor for AITs formation (Wacey et al., 2008b).
426 As is shown in Figs. 3h and 3j-3k, AITs radiate outward from a center rich in OM, suggesting that
427 the latter is necessary for the production of carbon dioxide, which leads to the propulsion of pyrite
428 through the calcium-phosphate host gel. Occurrence of AITs in phosphatized crustacean body
429 fossils in the Upper Cambrian of Northern Poland and Lower Devonian of Ukraine (Olempska and
430 Wacey, 2016) might represent an analogue of this type of pyritization and migration from
431 organic-rich centers. In other cases, pyrite crystals appear to migrate inward from an outer layer of
432 phosphatic granules (Figs. 3m-3p), which suggest production of pyrites during organic
433 degradation and sulfidization from sulfate reduction taking place in the intergranular pore spaces.
434 Similar phenomena have been reported in Zhang and Pratt (2008), but the authors interpreted them
435 as microborings produced by endolithic microorganisms. Although this possibility cannot be
436 entirely ruled out, the common presence of a terminal pyrite crystal and longitudinal striae (Figs.
437 3a, 3c, 3i and 4a-4d) favors the interpretation that these microstructures are likely to be AITs, and
438 can be more parsimoniously described as non-biological structures that require biological OM to
439 form.

440 5.3.2 A genetic classification scheme for AITs

441 Based on previously published data and our new observations, we propose a new genetic
442 classification scheme for AITs (Table 5). They are categorized into three types and further into five
443 subtypes. Those of type I are associated with single terminal pyrite crystals, with (I-a, Figs. 3d and

444 3f-3g) or without (I-b, Figs. 3c, 3i and 4a-4c) longitudinal striae.

445 Type II and type III AITs are interpreted to be produced by pyrite aggregates, including those
446 related to framboidal (II-a and II-b) and non-framboidal (III) pyrites. Examples for type II-a AIT
447 are relatively rare probably due to preservational effects or incomplete documentation. Olempska
448 and Wacey (2016) reported microtubes with a diameter ranging from 4 to 7.7 μm , which
449 terminated with framboidal rather than euhedral pyrite in the metacopine ostracod fossil from the
450 Lower Devonian of Podolia, Ukraine. This discovery led us to consider similar scenarios in the
451 Doushantuo phosphorites and other AIT-bearing successions. Possible AITs of this type include
452 single microtubes 2-10 μm wide, with crude longitudinal striae that are often separated by
453 inward-facing cusped ridges (Figs. 4b-d; and Zhang and Pratt, 2008, Fig. 3F). The close
454 correspondence between the spacings of longitudinal striae of AITs and the diameters of
455 micro-crystals in the framboids (Table 3 and Fig. 5) suggest that many of the AITs in the
456 Doushantuo phosphorites may be attributed to type II-a. Distinguishing type II-a AITs from type
457 I-b ones could be difficult when terminal pyrite framboid is not observed, but the inward-facing
458 cusped ridges (Figs. 4b-d), which mirrors the gaps between adjacent micro-crystals in framboid,
459 might serve as a diagnostic feature for the former. Type I-b AITs, by contrast, tend to display finer
460 striae with lower relief (Fig. 4a).

461 Disintegration of framboidal and non-framboidal pyrite clusters and their subsequent
462 migration might have produced dense clusters of AITs (types II-b and III) (Figs. 2i, 3a, 3d-3e and
463 3j-3k). Heavily clustered small microtubes of similar widths ranging from 0.4 to 1.5 μm , often
464 radiating from a central locus, have been reported previously from a few localities (Knoll and
465 Barghoorn, 1974, Fig. 2; Wacey et al., 2008b, Fig. 9d; Lepot et al., 2011, Fig. 5A; and Olempska

466 and Wacey, 2016, Figs. 5A and G-H) but their origin remains unexplained prior to the present
467 study.

468 We propose that consistent microtube widths within the typical range of framboid
469 micro-crystal (i.e., 0.4-1.5 μ m) in a star-burst AIT cluster may be used as a criteria to distinguish
470 type II-b AITs (e.g., Figs 5A and G-H in Olempska and Wacey, 2016) from type III AITs (Fig. 3e
471 in this study and Fig.3L in Schopf et al., 2010). Knoll and Barghoorn (1974) described AITs from
472 the Gunflint Formation and Fortescue Group and noticed that one group of AIT clusters have
473 consistent microtube width ranging between 0.5 and 0.8 μ m, which are one order of magnitude
474 smaller than the other AITs. These small AITs are here attributed to type II-b that are produced by
475 propulsion of disintegrated pyrite framboids. Depending on the number of micro-crystals in a
476 framboid, the number of microtubes in the resulting cluster of AITs can be variable (from dozens
477 to thousands) but would be difficult to measure with limited exposure in a thin section or on a
478 broken surface. The numerous AITs of variable sizes which radiate from the central organic-rich
479 nucleus in Figs. 3 m-n, however, could be produced by disintegration of either multiple framboidal
480 or non-framboidal aggregates.

481 5.3.3 A revised model for the genesis of AITs

482 Tyler and Barghoorn (1963) hypothesized that AITs were formed when pyrite grains were
483 propelled through solid rock by the force of crystallization of either quartz or carbonate in the
484 appendage. Knoll and Barghoorn (1974) later proposed that the propulsion force resulted from
485 pressure solution, which led to the movement of terminal grains. Thermal degradation of OM
486 attached to individual pyrite grains generates CO₂ and other gases, which in turn, would have built

487 up enough pressure to create compaction of the encompassing chert on the front face of the
488 moving pyrite grain. They noted however that cross-cutting relations of the trails to lithified
489 oncoids indicated that the matrix was lithified at the time the trails were formed. This model is
490 dependent upon the impermeability of the surrounding chert, which allowed pressure to build up
491 sufficiently to propel individual pyrite grains.

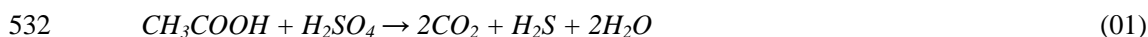
492 Wacey et al. (2008b) added some refinements to the Knoll and Barghoorn model by
493 suggesting that the (thermal) degassing of primary OM during early stages of diagenesis may have
494 been insufficient by itself to propel mineral grains, and that the biological activity of living
495 microbial communities may have assisted movement by locally increasing pH to promote silica
496 dissolution on the front face of the moving grains. This aspect of the model was based on a
497 reference to living experiments that claim to show silica dissolution by diatoms, heterotrophic
498 bacteria and cyanobacterial biofilms (Brehm et al., 2005). The ability of microorganisms to inhabit
499 the early diagenetic stage of deposition that produced AITs is not well-known however. Diatoms
500 did not evolve until the Mesozoic, so if their role in the microbial dissolution of silica in extant
501 settings is essential, support of this aspect of AIT formation would wane. As pointed out by Wacey
502 et al. (2008b) more experimental work will have to be done to ascertain the extent to which living
503 microbial communities were directly or indirectly essential for AIT formation.

504 The facts that AITs are filled with calcite whereas the cement between the apatite granules is
505 dolomite and that AITs never cut through the dolomitic cement (Figs. 3o, 3u and 4) suggest that
506 the formation and infilling of AITs took place before pervasive dolomite cementation during early
507 diagenesis. Considering the sub-micrometer size of apatite crystals and exceptional preservation of
508 microfossils in the Doushantuo phosphorites (e.g., Xiao et al., 1998; She et al., 2014), phosphate

509 crystallization must have been a rapid process during which diagenetic oxidation of OM could
510 have produced CO₂ gas. It is well known that biogenic gas can be trapped within microbial mats
511 and lead to gas domes during early diagenesis in modern environments (e.g., Gerdes et al., 1993).
512 Similar microbial mats or EPS preserved in phosphatic granules probably facilitated trapping of
513 gas during early diagenesis of the Doushantuo Formation. Moreover, the low permeability of
514 nanoscopic phosphate could have allowed pressure to build up inside the granules which
515 eventually led to propulsion of the pyrites. Therefore, we propose that propulsion of the pyrites
516 probably took place sometime between the initiation of apatite crystallization and the final
517 lithification of apatite granule.

518 The almost exclusive calcite infilling of AITs in the Doushantuo phosphorites is also notable.
519 We hypothesize that calcium carbonate precipitation in the Doushantuo AITs was a natural product
520 of organic decomposition during putrefaction of biomass, which is known to form gaseous CO₂ or
521 HCO₃⁻ in pore water solutions. Many microbial processes can be involved in putrefaction and
522 these contribute to the production of CO₂, however some non-biological processes may also be
523 involved in organic decomposition. During the post-glacial oxygenated world of the Doushantuo
524 Formation, sulfate was more abundant than before and was trapped as phosphate associated sulfate
525 in the apatite, such as in microfossiliferous granules of apatite in phosphorite from Yichang, as
526 detected by as trace by NanoSIMS (She et al., 2013). The corrosive effects of sulfuric acid on
527 biomass lead to the escape of CO₂ and hydrogen sulfide, which can conceivably form nano- to
528 micrometric pyrite if Fe²⁺ is present in solution. Since Ca²⁺ and Mg²⁺ were also present during
529 diagenesis as inferred from the co-occurrence of micron-size calcite flakes in AIT, massive
530 intergranular dolomite, and apatite in granules, we propose the following non-biological reaction

531 for the source of carbonate and hydrogen sulfide:



533 In this reaction, the reactants include humic acid represented by CH₃COOH (acetic acid) and
534 sulfuric acid, now preserved as kerogen and phosphate-associated sulfate, respectively. The
535 reaction products of this reaction are thus proposed to underlie the non-biological formation of
536 AITs from the products of the oxidation of biomass with sulfate reduction.

537 The H₂S then combines with dissolved ferrous iron to form colloidal FeS, which subsequently
538 converts to Fe₃S₄ (greigite) that is thermodynamically unstable relative to pyrite (Berner, 1967).
539 Fe₃S₄ aggregates into close-packed microcrystals, forming greigite framboids (Taylor, 1982).
540 Pyritization of the greigite through Fe loss is represented by the following reaction (Furukawa and
541 Barnes, 1995):



543 This leads to the formation of discrete euhedral pyrite grains or framboidal pyrites, depending
544 on the rate of pyritization (Wilkin and Barnes, 1996). Following the burial of the pyrites with the
545 phosphate containing OM, further oxidative degradation of the OM produces abundant CO₂ gas.
546 While the phosphatic gel was not fully lithified in order to allow plastic deformation, it was
547 sufficiently sealed and viscous to prevent CO₂ escape, thereby creating a pressure on the pyrite
548 and force it through the phosphate substrate. Propulsion of single pyrite crystals with smooth or
549 striated surfaces might have produced types I-a and I-b AITs, respectively, whereas propulsion of
550 intact pyrite framboids probably led to the formation of type II-a AITs (Table 5 and Fig. 8a). In
551 most cases, however, oxidation of OM inside pyrite framboids might have created local high
552 pressure environments in between microcrystals in the viscous gel, which could have led to the

553 eventual explosions of such framboids and produced type II-b AITs (Fig. 8b). Similar mechanism
554 may also apply to type III AITs. This model explains the formation of dense clusters of the
555 smallest AITs with similar diameters (equal to the diameter of the pyrite micro-crystals in
556 framboids) (e.g., Knoll and Barghoorn, 1974, Fig. 2; Lepot et al., 2011, Fig. 5A; and Olempska
557 and Wacey, 2016, Figs. 5A and G-H).

558 **6. Conclusions**

559 Abundant pyrite framboids and ambient inclusion trails have been documented from the
560 Doushantuo Formation in the Baizhu, Yichang, and Weng'an sections, South China. Pyrite
561 framboid size distributions in the black shale in Baizhu suggest that spatiotemporal redox
562 variations in the shallow marine environments, probably with frequent occurrence of euxinic
563 water columns stimulated by episodic cyanobacterial blooms, might have occurred during the
564 Doushantuo period and promoted phosphogenesis. While pyrite framboids also occur in granular
565 phosphorites of the Doushantuo Formation, they are more abundant in black shales, which do not
566 contain AITs because of the less viscous nature of the siliciclastic matrix.

567 AITs presented in this study and previous works may be distinguished from filamentous
568 microfossils and endolithic micro-borings with typical morphological features such as the
569 presence of a terminal mineral grain or cluster and longitudinal striae. We also propose additional
570 criteria for the recognition of AITs including the large variability of size, sharp outlines and
571 distinct infilling materials. AITs are then categorized into three types and further into five subtypes
572 (I-a, I-b, II-a, II-b, and III) based on their morphologies. Among these, types II AITs are
573 interpreted to be associated with framboidal pyrites. During early diagenesis, pyrites formed

574 primarily through non-biological oxidation of OM and reduction of phosphate-associated sulfate
575 in the presence of ferrous iron. Following the burial of pyrite framboids, accumulation of CO₂ gas
576 produced by oxidation of organic matter builds up the pressure and eventually drives the
577 movement of pyrite framboids, forming trails with striated walls in the viscous impermeable
578 matrix of fluorapatite. While biological processes may have participated in AIT formation, their
579 characteristics are more consistent with an indirect role by some microorganisms as well as a
580 requirement for abundant organic matter and a viscous gelatinous matrix for their formation.
581 Although it is unknown if AITs could form in similar context but only with non-biological organic
582 matter, AITs should be considered an indirect morphological and mineral biosignature.

583

584 **Acknowledgments:** The authors would like to acknowledge funding from National Natural
585 Science Foundation of China (grant # 41272038), Fundamental Research Funds for National
586 Universities, China University of Geosciences (Wuhan), State Key Laboratory of Biogeology and
587 Environmental Geology, China University of Geosciences (grant # GBL11610), and the 111
588 Program for the Ministry of Education of China and the State Administration of Foreign Expert
589 Affairs of China (grant # B07039). ZS and YZ thanks Xianquan Ping and Lianggai Yang for their
590 assistance in Raman microspectroscopic analysis and data processing, and Wenjing Xu, Zhuoma
591 Danzeng and Zhiyang Hou for their help in field work. DP acknowledges support from University
592 College London. The authors also thank two anonymous reviewers for their constructive
593 comments and editorial handling by D. Bottjer.

594

595

References:

596

597 Arning, E.T., Birgel, D., Brunner, B. and Peckmann, J., 2009. Bacterial formation of phosphatic
598 laminites off Peru. *Geobiology*, 7: 295-307.

599 Awramik, S.M., 1992. The oldest records of photosynthesis. *Photosynthesis Research*, 33: 75-89.

600 Awramik, S.M., Schopf, J.W. and Walter, M.R., 1983. Filamentous fossil bacteria from the Archean of
601 Western Australia. *Precambrian Research*, 20: 357-374.

602 Bailey, J.V., Joye, S.B., Kalanetra, K.M., Flood, B.E. and Corsetti, F.A., 2007. Evidence of giant
603 sulphur bacteria in Neoproterozoic phosphorites. *Nature*, 445: 198-201.

604 Baturin, G.N., Dubinchuk, V.T. and Zhegallo, E.A., 2000. Bacteria-like formations in phosphorites of
605 the Namibian shelf. *Oceanology*, 40: 737-741.

606 Benning, L.G., Wilkin, R.T. and Barnes, H.L., 2000. Reaction pathways in the Fe-S system below 100°
607 C. *Chemical Geology*, 167: 25-51.

608 Bernard, S., Beyssac, O. and Benzerara, K., 2008. Raman mapping using advanced line-scanning
609 systems: Geological applications. *Applied spectroscopy*, 62: 1180-1188.

610 Berner, R.A., 1967. Thermodynamic Stability of Sedimentary Iron Sulfides. *American Journal of*
611 *Science*, 265: 773-785.

612 Berner, R.A., 1985. Sulfate reduction, organic-matter decomposition and pyrite formation.
613 *Philosophical Transactions of the Royal Society A-Mathematical Physical and Engineering*
614 *Sciences*, 315: 25-38.

615 Beyssac, O., Goffe, B., Chopin, C. and Rouzaud, J.N., 2002. Raman spectra of carbonaceous material
616 in metasediments: a new geothermometer. *Journal of Metamorphic Geology*, 20: 859-871.

617 Bond, D.P.G. and Wignall, P.B., 2010. Pyrite framboid study of marine Permian – Triassic boundary

618 sections: A complex anoxic event and its relationship to contemporaneous mass extinction.
619 Geological Society of America Bulletin, 122: 1265-1279.

620 Brehm, U., Gorbushina, A. and Mottershead, D., 2005. The role of microorganisms and biofilms in the
621 breakdown and dissolution of quartz and glass. *Palaeogeography, Palaeoclimatology,*
622 *Palaeoecology*, 219: 117-129.

623 Condon, D., Zhu, M.Y., Bowring, S., Wang, W., Yang, A.H. and Jin, Y.G., 2005. U-Pb ages from the
624 Neoproterozoic Doushantuo Formation, China. *Science*, 308: 95-98.

625 Conway Morris, S. and Bengtson, S., 1994. Cambrian predators: possible evidence from boreholes.
626 *Journal of Paleontology*, 68: 1-23.

627 Cui, H., Kaufman, A.J., Xiao, S., Zhu, M., Zhou, C. and Liu, X., 2015. Redox architecture of an
628 Ediacaran ocean margin: Integrated chemostratigraphic ($\delta^{13}\text{C}$ - $\delta^{34}\text{S}$ - $^{87}\text{Sr}/^{86}\text{Sr}$ - Ce/Ce^*)
629 correlation of the Doushantuo Formation, South China. *Chemical Geology*, 405: 48-62.

630 Dong, Y., Ji, Q.Z. and Wang, S.H., 1984. The discovery of the trace fossils of microtubes in the rocks
631 of Sinian Doushantou Formation, South China. *Scientia Geologica Sinica*: 346-347.

632 Froelich, P.N., Arthur, M.A., Burnett, W.C., Deakin, M., Hensley, V., Jahnke, R., Kaul, L., Kim, K.H.,
633 Roe, K., Soutar, A., Vathakanon, C. and Aaramik, S.M., 1988. Early diagenesis of organic-matter
634 in peru continental margin sediments: Phosphorite precipitation. *Marine Geology*, 80: 309-343.

635 Furukawa, Y. and Barnes, H.L., 1995. Reactions forming pyrite from precipitated amorphous ferrous
636 sulfide. In: M.A. Vairavamurthy and M. Schoonen (Eds.), *ACS SYMPOSIUM SERIES*, pp.
637 194-205.

638 Gerdes, G., Claes, M., Dunajtschik-Piewak, K., Riege, H., Krumbein, W.E. and Reineck, H.E., 1993.
639 Contribution of microbial mats to sedimentary surface structures. *Facies*, 29: 61-74.

640 Guan, C., Zhou, C., Wang, W., Wan, B., Yuan, X. and Chen, Z., 2014. Fluctuation of shelf basin redox
641 conditions in the early Ediacaran: Evidence from Lantian Formation black shales in South China.
642 *Precambrian Research*, 245: 1-12.

643 Huang, Q., 1989. The characteristics of phosphates in Baizhu phosphorus mine, Baokang city, Hubei
644 province. *Geology of Chemical Minerals*: 91-99.

645 Jiang, G.Q., Shi, X.Y., Zhang, S.H., Wang, Y. and Xiao, S.H., 2011. Stratigraphy and paleogeography
646 of the Ediacaran Doushantuo Formation (ca. 635-551 Ma) in South China. *Gondwana Research*, 19:
647 831-849.

648 Kendall, B., Creaser, R.A. and Selby, D., 2009. 187Re-187Os geochronology of Precambrian
649 organic-rich sedimentary rocks. *Geological Society London Special Publications*, 326: 85-107.

650 Knoll, A.H. and Barghoorn, E.S., 1974. Ambient pyrite in precambrian chert: new evidence and a
651 theory. *Proceedings of the National Academy of Sciences*, 71: 2329-31.

652 Knudsen, A.C. and Gunter, M.E., 2002. Sedimentary phosphorites - An example: Phosphoria formation,
653 southeastern Idaho, USA. *Phosphates: Geochemical, Geobiological, and Materials Importance*, 48:
654 363-389.

655 Kouketsu, Y., Mizukami, T., Mori, H., Endo, S., Aoya, M., Hara, H., Nakamura, D. and Wallis, S.,
656 2014. A new approach to develop the Raman carbonaceous material geothermometer for low-grade
657 metamorphism using peak width. *Island Arc*, 23: 33-50.

658 Lahfid, A., Beyssac, O., Deville, E., Negro, F., Chopin, C. and Goffé, B., 2010. Evolution of the
659 Raman spectrum of carbonaceous material in low-grade metasediments of the Glarus Alps
660 (Switzerland). *Terra Nova*, 22: 354-360.

661 Lepot, K., Benzerara, K. and Philippot, P., 2011. Biogenic versus metamorphic origins of diverse

662 microtubes in 2.7Gyr old volcanic ashes: Multi-scale investigations. *Earth and Planetary Science*
663 *Letters*, 312: 37-47.

664 Lepot, K., Philippot, P., Benzerara, K. and Wang, G.Y., 2009. Garnet-filled trails associated with
665 carbonaceous matter mimicking microbial filaments in Archean basalt. *Geobiology*, 7: 393-402.

666 Li, C., Love, G.D., Lyons, T.W., Fike, D.A., Sessions, A.L. and Chu, X.L., 2010. A stratified redox
667 model for the Ediacaran ocean. *Science*, 328: 80-83.

668 Li, C., Planavsky, N.J., Shi, W., Zhang, Z., Zhou, C., Cheng, M., Tarhan, L.G., Luo, G. and Xie, S.,
669 2015. Ediacaran Marine Redox Heterogeneity and Early Animal Ecosystems. *Scientific Reports*, 5:
670 17097.

671 Liu, P.J. and Yin, C.Y., 2006. Enigmatic Microtunnels—The Drag Marks of Pyrites on the
672 Phosphatized Spheroidal Fossils from Sinian Doushantuo Formation at Weng'an, Guizhou Province.
673 *Geological Review*, 52: 11-14.

674 Liu, P.J., Yin, C.Y., Gao, L.Z., Tang, F. and Chen, S.M., 2009. New material of microfossils from the
675 Ediacaran Doushantuo Formation in the Zhangcunping area, Yichang, Hubei Province and its
676 zircon SHRIMP U-Pb age. *Chinese Science Bulletin*, 54: 1058-1064.

677 McLoughlin, N., Brasier, M.D., Wacey, D. and Perry, R.S., 2007. On biogenicity criteria for endolithic
678 microborings on early Earth and beyond. *Astrobiology*, 7: 10-26.

679 Nielsen, J.K. and Shen, Y., 2004. Evidence for sulfidic deep water during the Late Permian in the East
680 Greenland Basin. *Geology*, 32: 1037-1040.

681 Olempska, E. and Wacey, D., 2016. Ambient inclusion trails in Palaeozoic crustaceans
682 (Phosphatocopina and Ostracoda). *Palaeogeography, Palaeoclimatology, Palaeoecology*, 441, Part 4:
683 949-958.

684 Papineau, D., De Gregorio, B.T., Cody, G.D., Fries, M.D., Mojzsis, S.J., Steele, A., Stroud, R.M. and
685 Fogel, M.L., 2010. Ancient graphite in the Eoarchean quartz-pyroxene rocks from Akilia in
686 southern West Greenland I: Petrographic and spectroscopic characterization. *Geochimica et*
687 *Cosmochimica Acta*, 74: 5862-5883.

688 Papineau, D., Gregorio, B.D., Fearn, S., Kilcoyne, D., McMahon, G., Purohit, R. and Fogel, M., 2016.
689 Nanoscale petrographic and geochemical insights on the origin of the Palaeoproterozoic
690 stromatolitic phosphorites from Aravalli Supergroup, India. *Geobiology*, 14: 3-32.

691 Papineau, D., Purohit, R., Fogel, M.L. and Shields-Zhou, G.A., 2013. High phosphate availability as a
692 possible cause for massive cyanobacterial production of oxygen in the Paleoproterozoic atmosphere.
693 *Earth and Planetary Science Letters*, 362: 225-236.

694 Schopf, J.W., Kudryavtsev, A.B., Sugitani, K. and Walter, M.R., 2010. Precambrian microbe-like
695 pseudofossils: A promising solution to the problem. *Precambrian Research*, 179: 191-205.

696 Schulz, H.N. and Schulz, H.D., 2005. Large sulfur bacteria and the formation of phosphorite. *Science*,
697 307: 416-418.

698 She, Z., Strother, P. and Papineau, D., 2014. Terminal Proterozoic cyanobacterial blooms and
699 phosphogenesis documented by the Doushantuo granular phosphorites II: Microbial diversity and C
700 isotopes. *Precambrian Research*, 251: 62-79.

701 She, Z., Strother, P., McMahon, G., Nittler, L.R., Wang, J., Zhang, J., Sang, L., Ma, C. and Papineau,
702 D., 2013. Terminal Proterozoic cyanobacterial blooms and phosphogenesis documented by the
703 Doushantuo granular phosphorites I: In situ micro-analysis of textures and composition.
704 *Precambrian Research*, 235: 20-35.

705 Slansky, M., 1986. *Geology of Sedimentary Phosphates*. North Oxford Academic, London.

706 Strother, P.K. and Tobin, K., 1987. Observations on the genus *Huroniospora* Barghoorn: Implications
707 for paleoecology of the Gunflint microbiota. *Precambrian Research*, 36: 323-333.

708 Taylor, G.R., 1982. A mechanism for framboid formation as illustrated by a volcanic exhalative
709 sediment. *Mineralium Deposita*, 17: 23-36.

710 Tiwari, M. and Siddaiah, N.S., 2012. Ambient Inclusion Trails (AITs) from the Neoproterozoic
711 Gangolihat Formation, Lesser Himalaya, India. *Palaeoworld*, 21: 92-99.

712 Tyler, S.A. and Barghoorn, E.S., 1963. Ambient pyrite grains in Precambrian cherts. *American Journal*
713 *of Science*, 261: 424-432.

714 Wacey, D., Kilburn, M., Stoakes, C., Aggleton, H. and Brasier, M., 2008b. Ambient Inclusion Trails:
715 Their Recognition, Age Range and Applicability to Early Life on Earth. In: Y. Dilek, H. Furnes and
716 K. Muehlenbachs (Eds.), *Links Between Geological Processes, Microbial Activities & Evolution of*
717 *Life*. Springer Science + Business Media B.V, pp. 113-134.

718 Wacey, D., Kilburn, M.R., McLoughlin, N., Parnell, J., Stoakes, C.A., Grovenor, C.R.M. and Brasier,
719 M.D., 2008a. Use of NanoSIMS in the search for early life on Earth: ambient inclusion trails in a *c.*
720 3400 Ma sandstone. *Journal of the Geological Society*, 165: 43-53.

721 Wacey, D., Kilburn, M.R., Saunders, M., Cliff, J.B., Kong, C., Liu, A.G., Matthews, J.J. and Brasier,
722 M.D., 2015. Uncovering framboidal pyrite biogenicity using nano-scale CN org mapping. *Geology*,
723 43: 27-30.

724 Wang, L., Shi, X. and Jiang, G., 2012. Pyrite morphology and redox fluctuations recorded in the
725 Ediacaran Doushantuo Formation. *Palaeogeography, Palaeoclimatology, Palaeoecology*, 333-334:
726 218-227.

727 Wignall, P.B. and Newton, R., 1998. Pyrite framboid diameter as a measure of oxygen deficiency in

728 ancient mudrocks. *American Journal of Science*, 298: 537-552.

729 Wilkin, R.T. and Arthur, M.A., 2001. Variations in pyrite texture, sulfur isotope composition, and iron
730 systematics in the Black Sea: Evidence for Late Pleistocene to Holocene excursions of the O₂-H₂S
731 redox transition. *Geochimica et Cosmochimica Acta*, 65: 1399-1416.

732 Wilkin, R.T. and Barnes, H.L., 1996. Pyrite formation by reactions of iron monosulfides with dissolved
733 inorganic and organic sulfur species. *Geochimica et Cosmochimica Acta*, 60: 4167-4179.

734 Wilkin, R.T. and Barnes, H.L., 1997. Pyrite formation in an anoxic estuarine basin. *American Journal*
735 *of Science*, 297: 620-650.

736 Wilkin, R.T., Arthur, M.A. and Dean, W.E., 1997. History of water-column anoxia in the Black Sea
737 indicated by pyrite framboid size distributions. *Earth and Planetary Science Letters*, 148: 517-525.

738 Wilkin, R.T., Barnes, H.L. and Brantley, S.L., 1996. The size distribution of framboidal pyrite in
739 modern sediments: An indicator of redox conditions. *Geochimica et Cosmochimica Acta*, 60:
740 3897-3912.

741 Xiao, S., McFadden, K.A., Peek, S., Kaufman, A.J., Zhou, C., Jiang, G. and Hu, J., 2012. Integrated
742 chemostratigraphy of the Doushantuo Formation at the northern Xiaofenghe section (Yangtze
743 Gorges, South China) and its implication for Ediacaran stratigraphic correlation and ocean redox
744 models. *Precambrian Research*, 192-195: 125-141.

745 Xiao, S., Zhang, Y. and Knoll, A.H., 1998. Three-dimensional preservation of algae and animal
746 embryos in a Neoproterozoic phosphorite. *Nature*, 391: 553-558.

747 Xiao, S., Zhou, C., Liu, P., Wang, D. and Yuan, X., 2014. Phosphatized acanthomorphic acritarchs and
748 related microfossils from the Ediacaran Doushantuo Formation at Weng'an (South China) and their
749 implications for biostratigraphic correlation. *Journal of Paleontology*, 88: 1-67.

- 750 Xiao, S.H. and Knoll, A.H., 1999. Fossil preservation in the Neoproterozoic Doushantuo phosphorite
751 Lagerstätte, South China. *Lethaia*, 32: 219-240.
- 752 Zhang, S., Jiang, G. and Han, Y., 2008. The age of the Nantuo Formation and Nantuo glaciation in
753 South China. *Terra Nova*, 20: 289 – 294.
- 754 Zhang, X. and Pratt, B.R., 2008. Microborings in Early Cambrian phosphatic and phosphatized fossils.
755 *Palaeogeography, Palaeoclimatology, Palaeoecology*, 267: 185-195.
- 756 Zhang, Z., 1984. Appendaged pyrite in the Sinian of South China. *Chinese Science Bulletin*, 28:
757 1253-1255.
- 758 Zhou, C., Yuan, X., Xiao, S., Chen, Z. and Xue, Y., 2004. Phosphatized fossil assemblage from the
759 Doushantuo Formation in Baokang, Hubei province. *Acta Micropalaeontologica Sinica*, 21:
760 349-366.
- 761 Zhu, B., Becker, H., Jiang, S., Pi, D., Fischer-Gödde, M. and Yang, J., 2013. Re – Os geochronology of
762 black shales from the Neoproterozoic Doushantuo Formation, Yangtze platform, South China.
763 *Precambrian Research*, 225: 67-76.
- 764

765 **Figure captions**

766 Fig. 1 Geological map and stratigraphic column. (a), Simplified geological map of the study
767 area during the early Ediacaran Period. Inset shows the geographic location of the Yangtze Block.
768 Locations of the Baizhu and Taopinghe sections are indicated. (b), Measured stratigraphic column
769 of the Doushantuo Formation in Baizhu showing sampled horizons. NT: Nantuo Formation; DY:
770 Dengying Formation.

771

772 Fig. 2 Structures and microstructures of the Doushantuo phosphorites and the occurrences of
773 AITs. (a-c), Outcrops of phosphorites: (a), Banded phosphorite; (b), Stromatolitic and lenticular
774 phosphorite; (c), Concretionary phosphorite. (d), Intraclastic phosphorite containing detrital quartz
775 (qtz) and carbonate (carb) and phosphatic (apa) intraclasts that are cemented by transparent
776 phosphatic groundmass, transmitted light (TL). (e), Banded phosphorite showing intercalation of
777 finely laminated organic-rich layers and silica-cemented granular layers, scanned image of a thin
778 section. (f), Close-up view of the granular layer in (e) showing organically-zoned micro-oncoids
779 (TL). (g), Banded phosphorite showing dark organic-rich phosphatic stripes (apa) and transparent
780 dolomitic layers (dol), scanned image of a thin section. (h), Enlarged view of the marked area in (g)
781 showing granular-clotted texture in the dark phosphatic stripe, (TL). (i), An AIT with an oxidized
782 terminal pyrite crystal observed in a phosphatic granule; note that the trail appears to follow the
783 margin of the granule. (j), Alternating light and dark laminae in a stromatolite-like structure. (k),
784 Abundant AITs in massive cryptocrystalline apatite. (l), Numerous AITs in isotropic substrate in a
785 banded phosphorite (d), the high-order white interference color indicating filling of the AITs with
786 carbonate minerals, crossed nicols (XPL). All images are obtained from the Baizhu samples,
787 except for (i) which is from a Taopinghe phosphorite.

788

789 Fig. 3 Photomicrographs and Raman hyperspectral images of AITs and associated pyrites in
790 the Doushantuo phosphorites. (a), Curved and twisted AITs filled with carbonate. (b),
791 Longitudinal section of a spiral AIT (center of the image) in a phosphatic granule; notice terminal
792 pyrite grain which is of comparable size as the spiral AIT (arrow). (c), Longitudinal striae
793 following angular pyrite crystals. (d), AITs cross-cutting phosphatic granules (arrows), limonite

794 coating clearly visible on the wall of the tubes. (e), AITs radiating from a central locus; note the
795 hollow microtube of the AIT in the bottom right corner and the presence of a oxidized pyrite
796 cluster (framboid?) at the terminus of the microtube near the bottom left corner (arrowed). (f),
797 Oxidized hexagonal terminal pyrites (arrows) and associated microtubes. (g-h), possible partially
798 oxidized pyrite framboids in interstitial quartz cement in a granular phosphorite. (i) a well
799 preserved pyrite framboid (apparent diameter = 5.8 microns) in phosphatic granule. (j) Bend of an
800 AIT caused by collision with another terminal pyrite (arrowed). (k), AITs radiating from an
801 organic-rich center in different directions (arrows). (l), A cubic pyrite crystal followed by a striated
802 trail (oblique section); inset is the reflected light image of the pyrite at the same scale. (m-o),
803 "Starburst" type AITs: (m), numerous AITs radiating outward from an organic-rich mass in a
804 phosphatic granule, arrow showing the moving direction of pyrites; (n), sketch of the clearest AITs
805 in Fig. 3m and (o), Raman hyperspectral image of apatite (turquoise), organic matter (OM, red),
806 interstitial dolomite cement (green), and calcite infillings (purple) in AITs for the marked area in
807 (m). (p-u), Inward migrated AITs. (p), Abundant anhedral pyrites in a granule, some followed with
808 trails of equal diameters; arrows indicate the direction of pyrite movements. (q-s), AITs filled with
809 carbonate minerals which are clearly recognized by their high-order white interference colors. (s),
810 Close-up of the marked area in (r) showing the inward migration (arrowed) of pyrite from outside
811 or the outer envelope of a granule. (t), Corresponding reflected light image of the pyrites. (u),
812 Raman hyperspectral image of apatite (turquoise), organic matter (OM, red), interstitial dolomite
813 cement (green), and calcite infillings (purple) in AITs, same area as (r). In (o) and (u), pyrites were
814 not detected because the laser energy was too low (1mW). Transmitted light, crossed nicols: (a)
815 and (p-s); transmitted light, plane polarized: (b-g), (j-k), (m), (p) and (s); Reflected light: (h-i), (l)
816 and (t). (a), (c) and (j): Baizhu samples; (b), (k) and (m-u): Weng'an samples; (d-i) and (l):
817 Taopinghe sample.

818

819 Fig. 4 Secondary electron images of typical microstructures of AITs and pyrite framboids: (a),
820 Part of a microtube showing fine longitudinal striae; note the nearly right angle of the walls of the
821 microtube (arrowed). (b-d), Inward-facing cusped longitudinal ridges (crude striae) on the wall of
822 AITs, note the AIT in (c) exhibiting a spiral shape. (e), Casts of the microtubes of two AITs; notice

823 the longitudinal ridges that correspond to the striae in (a) and the square cross section of the upper
824 cast (arrowed). (f), Porous calcite flakes filling a microtube. (g), Cross sections of AITs. (h-i)
825 Pyrite framboid composed of cubic micro-crystals; notice that a thin membrane covers each of the
826 micro-crystals in (i). (j-k) Pyrite micro-crystals showing dodecahedron habit. (l) Pyrite framboid
827 composed of subhedral micro-crystals. (m) Framboid coated with a thin layer of amorphous
828 material. (n) A cluster of euhedral pyrites with flat crystal surface. (o) Parallel aligned framboids
829 in the dark laminae. All images were obtained with the secondary electron (SE) mode, except for
830 (h), (j) and (o) which were taken using the backscattered electron (BSE) mode. (a) and (e) are
831 from the Weng'an samples (granular phosphorites), others are from the Baizhu samples (b-d and
832 f-g: phosphorites, h-o: black shales).

833

834 Fig. 5 Comparison of sizes of AITs and pyrite framboids. D_{frm} and d_{frm} refer to the diameters of
835 framboid and micro-crystals, respectively. D_{AIT} and d_{AIT} refer to the diameters of the microtube
836 and the spacing of longitudinal striae, respectively.

837

838 Fig. 6 Raman spectra of apatite, organic matter and carbonate minerals of various occurrences
839 in the Doushantuo phosphorites.

840

841 Fig. 7 Stratigraphic distribution of pyrite morphology for the Baizhu section. Pyrite
842 morphotypes: 0 — negligible pyrites; Py — only non-framboidal pyrites; Frm — both
843 non-framboidal and framboidal pyrites. MFD, maximum framboid diameter.

844

845 Fig. 8 A new model for the formation of type II AITs.

Table 1 The occurrences and mineralogical context of AITs in the Baizhu phosphorites

Host rock lithology	Distribution of AITs	Diameter of AITs	Terminal grains	Infilling mineral	Longitudinal striae	Organic matter	Horizon number
Organic-rich banded phosphorite	Light-colored phosphatic band	1-10 μm	Pyrite	Iron oxide, organic matter	Present	Abundant	8,14,23
Granular layer in banded phosphorite	Light-colored intergranular cement	9-68 μm	Iron oxide	Calcite	Present	Rare	10
Intraclastic phosphorite	Light-colored interstitial cement	2-44 μm	Iron oxide	Calcite	Present	Rare	9,12
Concretionary phosphorite	Phosphatic laminae	5-12 μm	Iron oxide, pyrite	Iron oxide, organic matter	Present	Abundant	11,12
Stromatolitic phosphorite	Phosphatic laminae	4-56 μm	Iron oxide	Calcite	Present	Common	5,12

847 **Table 2 Sizes of pyrite framboids and micro-crystals and width of AITs and spacings of their longitudinal striae**

Pyrite framboids						AITs					
Sample Number	D_{frm} (μm)	d_{frm} (μm)	Sample Number	D_{frm} (μm)	d_{frm} (μm)	Sample Number	D_{frm} (μm)	d_{frm} (μm)	Sample Number	D_{AIT} (μm)	d_{AIT} (μm)
BK13-1-1	4.5	0.9	BK13-1-11	2.9	0.8	BK17-1-4	8.1	1.2	BK11-2	1.6	0.3
BK13-1-2	4.1	0.7	BK13-1-12	3.7	1.0	BK17-1-5	5.7	1.0	BK14-2-1	2.4	0.5
BK13-1-3	6.0	1.0	BK13-1-13	3.5	0.7	BK17-1-6	9.8	1.2	BK14-2-2	2.1	0.3
BK13-1-4	4.7	0.5	BK13-1-14	4.0	1.0	BK17-2-1	3.4	0.5	BK14-2-3	4.4	1.1
BK13-1-5	2.2	0.6	BK13-1-15	3.1	0.7	BK17-2-2	5.8	1.1	1*	9.7	1.9
BK13-1-6	6.5	1.0	BK13-1-16	6.9	0.8	BK17-2-3	9.2	1.2	2*	3.2	0.8
BK13-1-7	7.4	1.5	BK13-1-17	4.6	0.7	BK17-2-4	3.1	0.5	3*	7.0	1.5
BK13-1-8	6.4	1.4	BK17-1-1	6.8	0.8	BK17-2-5	4.7	0.9	4*	6.2	1.1
BK13-1-9	5.0	1.1	BK17-1-2	3.9	0.4	BK17-2-6	2.2	0.4	5*	5.7	0.9
BK13-1-10	4.9	1.1	BK17-1-3	6.4	1.2				6*	5.3	1.0

848 Data marked with * was measured from Fig. 14 in Wacey et al., 2008b. D_{frm} and d_{frm} refer to the diameter of individual framboids and mean diameter (n=5) of micro-crystals in the

849 respective framboid, respectively. D_{AIT} and d_{AIT} refer to the diameters of the microtube and the spacing of longitudinal striations (mean value of 3 to 5 measurements), respectively.

Table 3 Size distributions of pyrite framboids in the Baizhu samples

Sample Number	H (m)	n	d _{MIN} (μm)	d _{MAX} (μm)	D _{MEAN} (μm)	S.D. (μm)	R _D	R _F
BK8-1	11.3	214	1.6	7.3	3.8	1.0	12%	45%
BK13-1	25.6	231	1.6	7.4	4.1	1.0	18%	80%
BK14-2	28.6	200	1.7	6.7	3.3	0.9	4%	20%
BK17-1	32.9	194	1.8	9.3	4.5	1.7	29%	30%
BK17-2	33.4	236	1.0	10.8	3.6	1.4	16%	70%
BK20-2	40.8	194	0.9	7.8	3.2	1.3	10%	30%
BK20-3	41.7	200	1.3	7.7	3.0	1.0	5%	25%
BK20-4	41.9	207	1.4	7.5	3.0	1.0	4%	40%
BK23-1	49.1	200	1.3	6.9	3.7	1.2	14%	50%

851 Abbreviations: H - the stratigraphic level of sampling locality from the base of the Doushantuo Formation. "n"
852 - the number of framboidal pyrites analyzed. "d_{MIN}", "d_{MAX}" and "d_{MEAN}" - minimum, maximum and mean
853 diameter of framboidal pyrites, respectively. S.D. - standard deviation of framboid diameters. "R_D" - percentage of
854 pyrite framboids with diameter $\geq 10 \mu\text{m}$ in the total pyrite framboids. "R_F" - the areal ratio of pyrite framboids to
855 all pyrites.

856 **Table 4 Raman spectral characteristics and estimated temperatures for the Doushantuo phosphorites in Baizhu**

Sample Number	G			D1			D2			D3		D4		RA1	RA2	T1 (°C)	T2 (°C)
	Position	FWHM	Area	Position	FWHM	Area	Position	FWHM	Area	Position	Area	Position	Area				
BK10-14-2	1598.1	40.8	1237.9	1343.6	73.2	4032.5	1616.9	24.5	574.1	1533.6	1018.0	1219.7	1303.3	0.65	1.89	347	359
BK15-1_01	1599.3	41.8	761.6	1344.3	87.7	2644.1	1619.0	26.4	422.8	1530.9	633.7	1210.6	534.8	0.64	1.75	325	329
BK10-8-2_01	1601.8	44.4	17954.3	1349.8	55.9	38343.6	1625.3	20.8	4754.3	1520.9	13234.6	1285.4	23742.1	0.63	1.73	322	324
BK10-8-2_02	1601.7	44.0	17787.9	1349.8	52.1	34088.0	1625.2	21.0	4892.8	1530.0	9267.2	1315.0	33603.1	0.68	2.12	379	411
BK10-8-3_03	1600.2	44.9	2760.0	1342.1	114.8	9420.8	1619.4	27.3	1134.0	1535.0	2507.9	1203.2	1505.4	0.63	1.71	318	319
ZK511-32_01	1590.1	59.0	5227.7	1347.8	142.2	17593.8	1611.9	33.3	4123.6	1499.3	4054.3	1233.4	3247.3	0.61	1.55	291	285

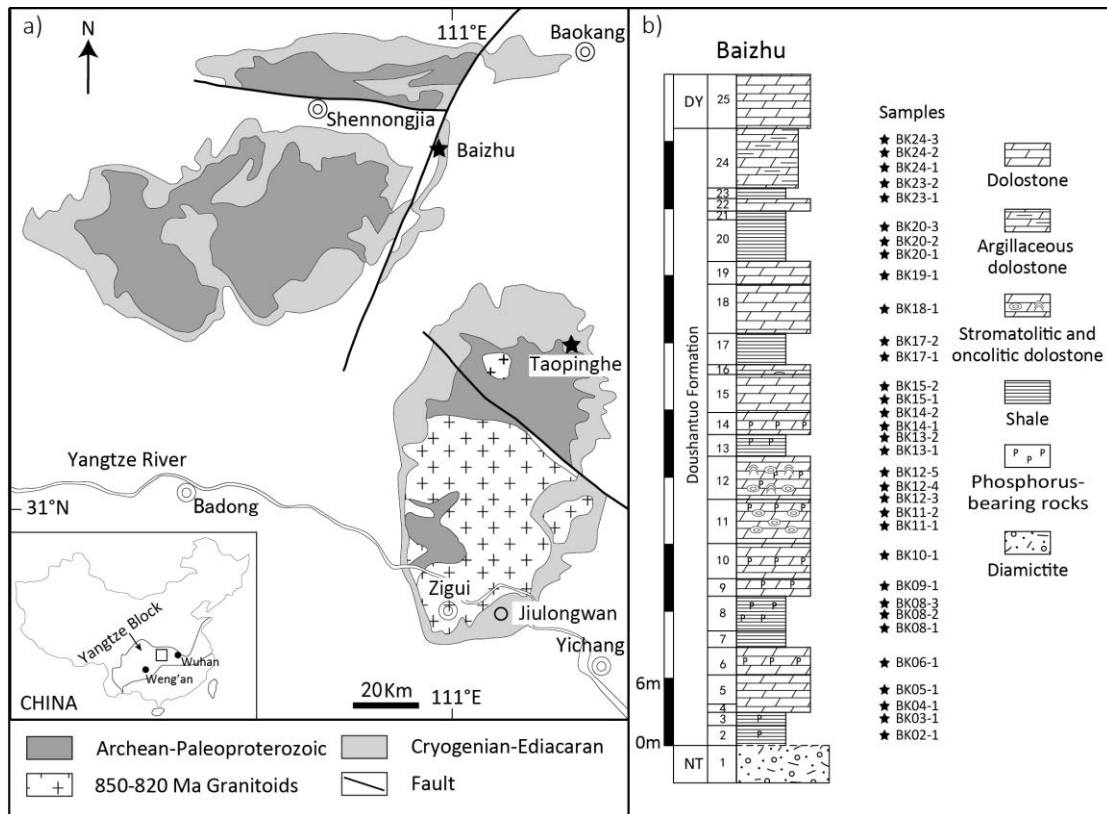
857 Raman spectral parameters (RA1 and RA2) and respective temperatures (T1 and T2) were calculated using the equations proposed for low-grade metasediments

858 by Lahfid et al. (2010).

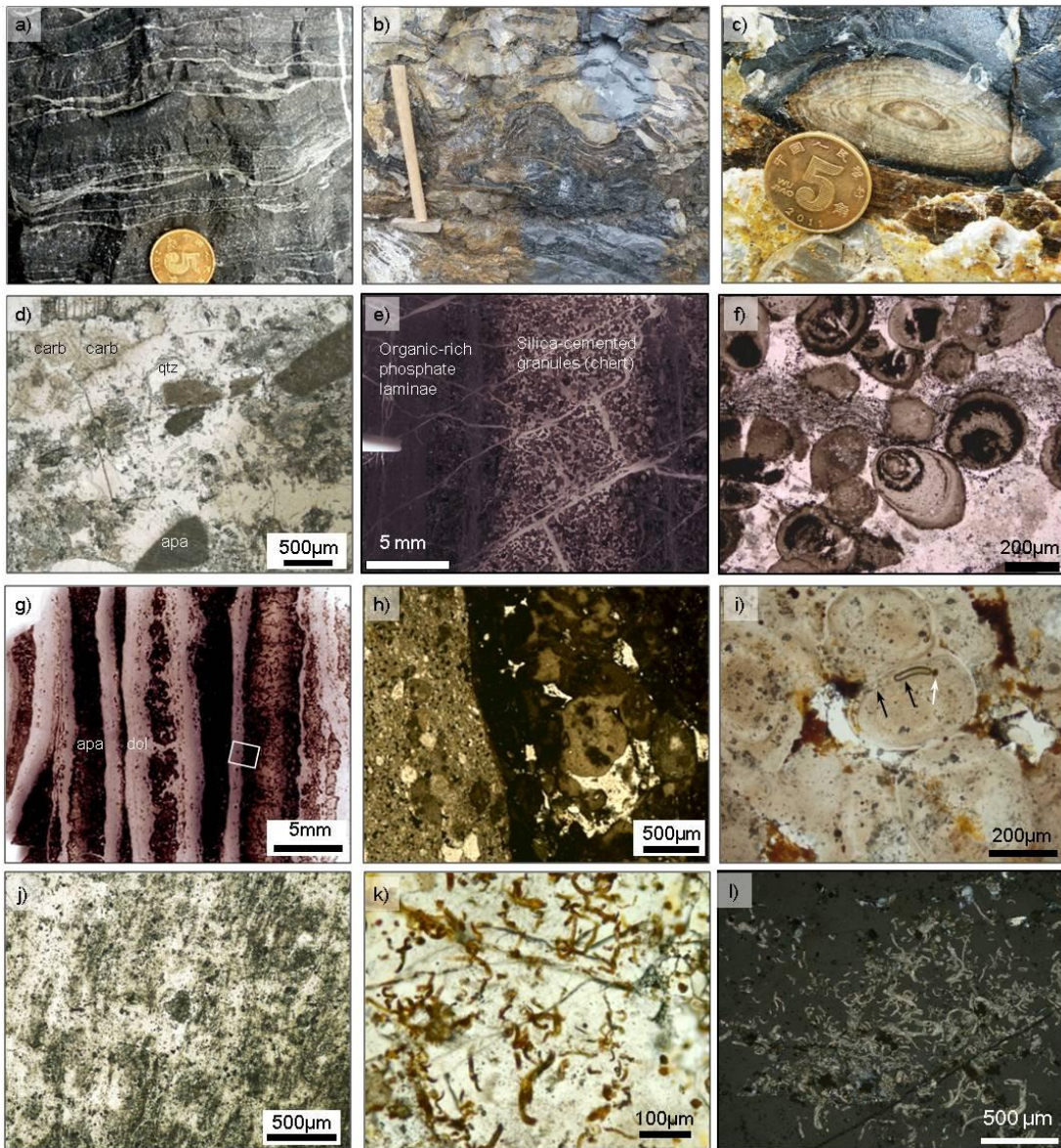
859 **Table 5 A genetic classification scheme of AITs based on morphological features and**
 860 **associated pyrites**

Types	AIT morphology	Associated pyrites (interpretation)
I-a	Non-striated single microtubes with variable widths	Smooth single crystals, euhedral to anhedral
I-b	Finely striated single microtubes with variable widths	Striated single crystals, euhedral to anhedral
II-a	Single microtubes 2-10 μm wide, with longitudinal striae often separated by inward-facing cusped ridges	Intact framboids generally 2-10 μm in diameter
II-b	Star-burst type AITs with microtubes of comparable widths (0.4-1.5 μm)	Micro-crystals from disintegrated framboids
III	Cluster of microtubes with variable widths	Non-framboidal aggregates

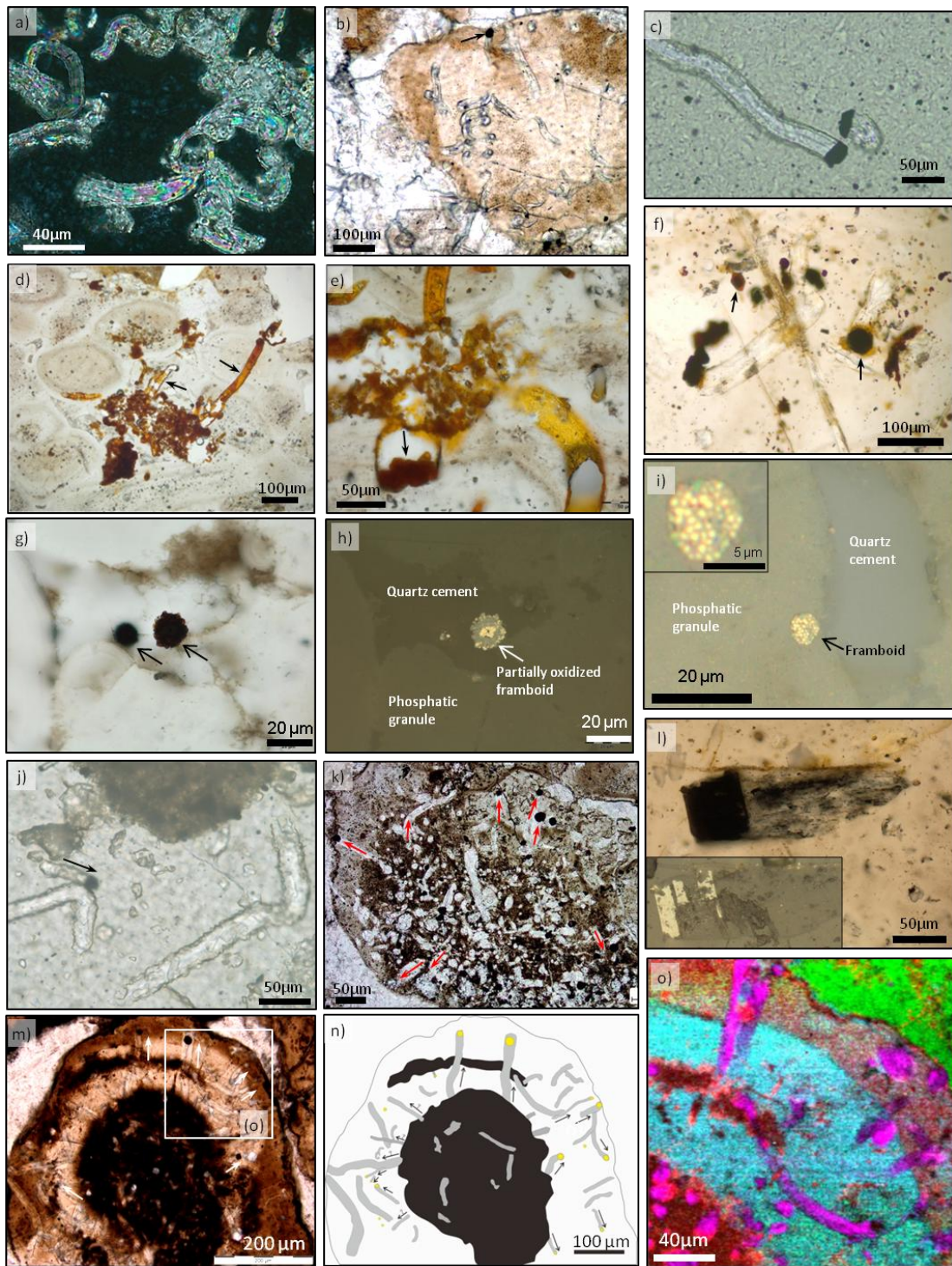
861

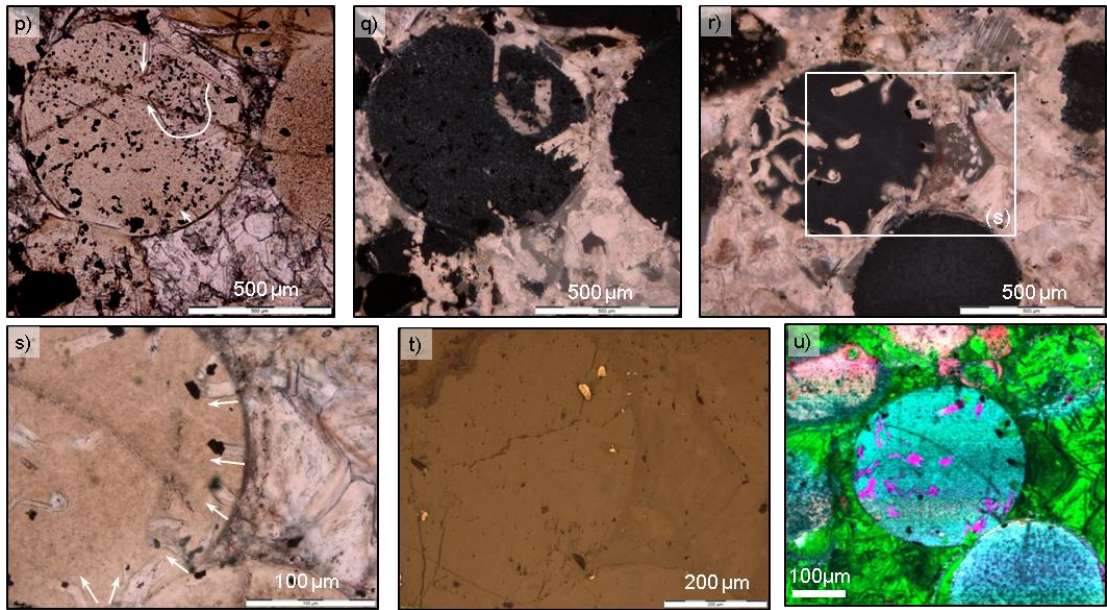


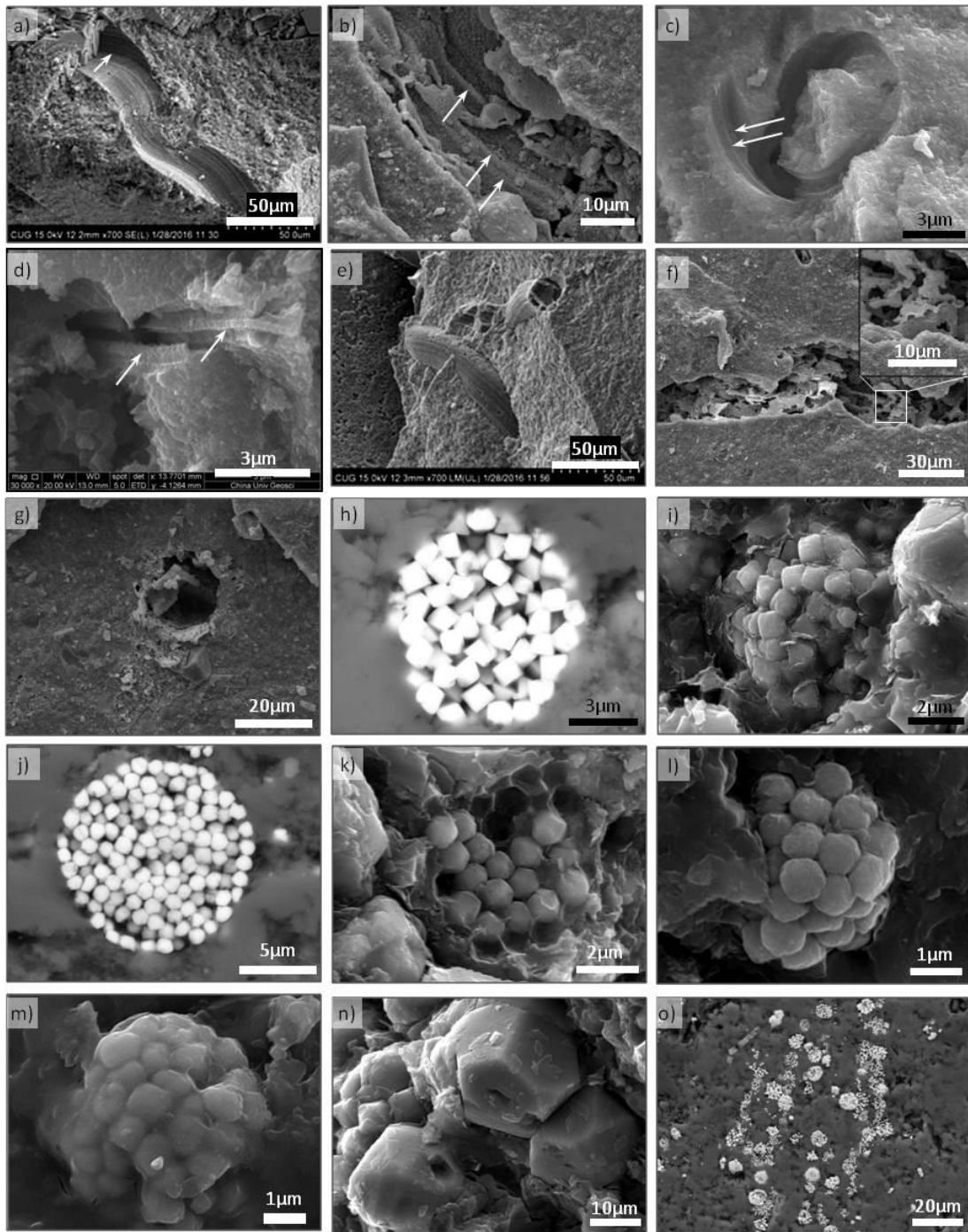
864 Figure 2_2 columns_black-and-white

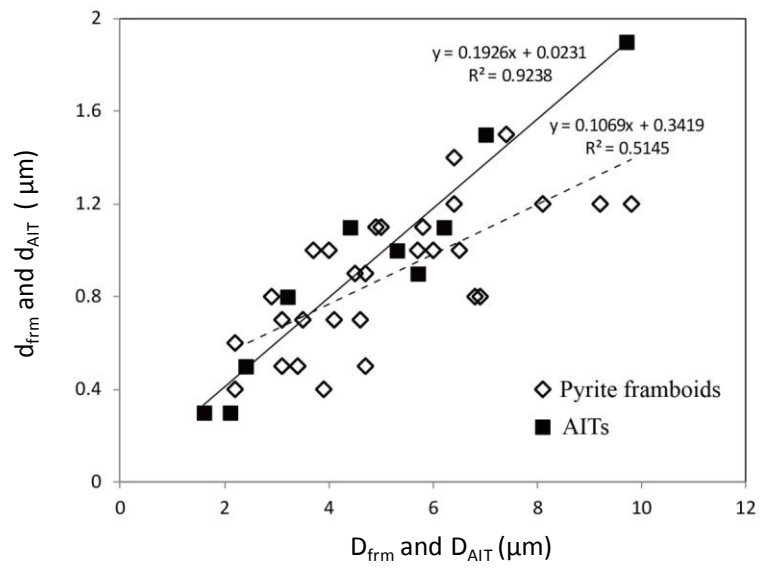


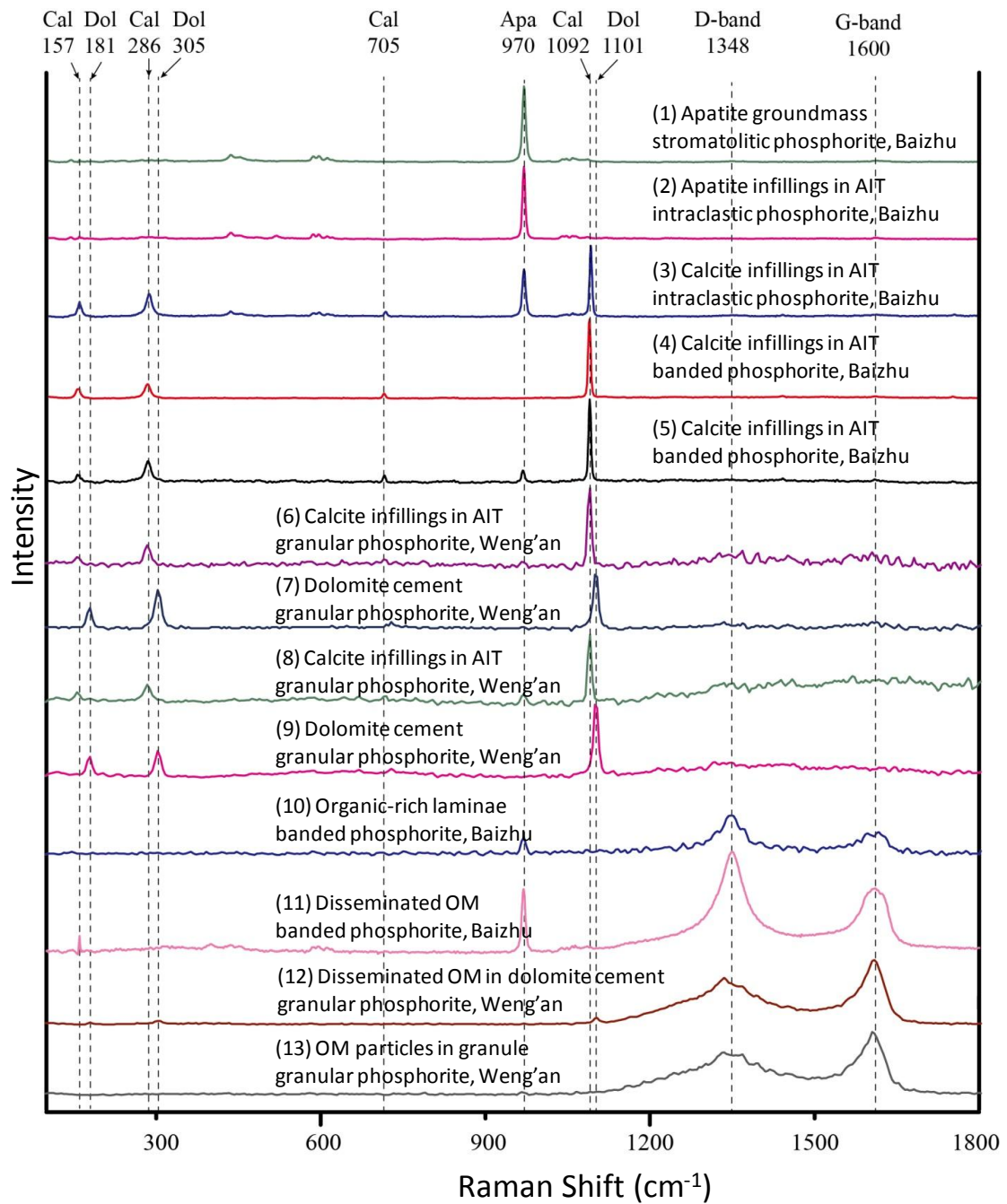
865

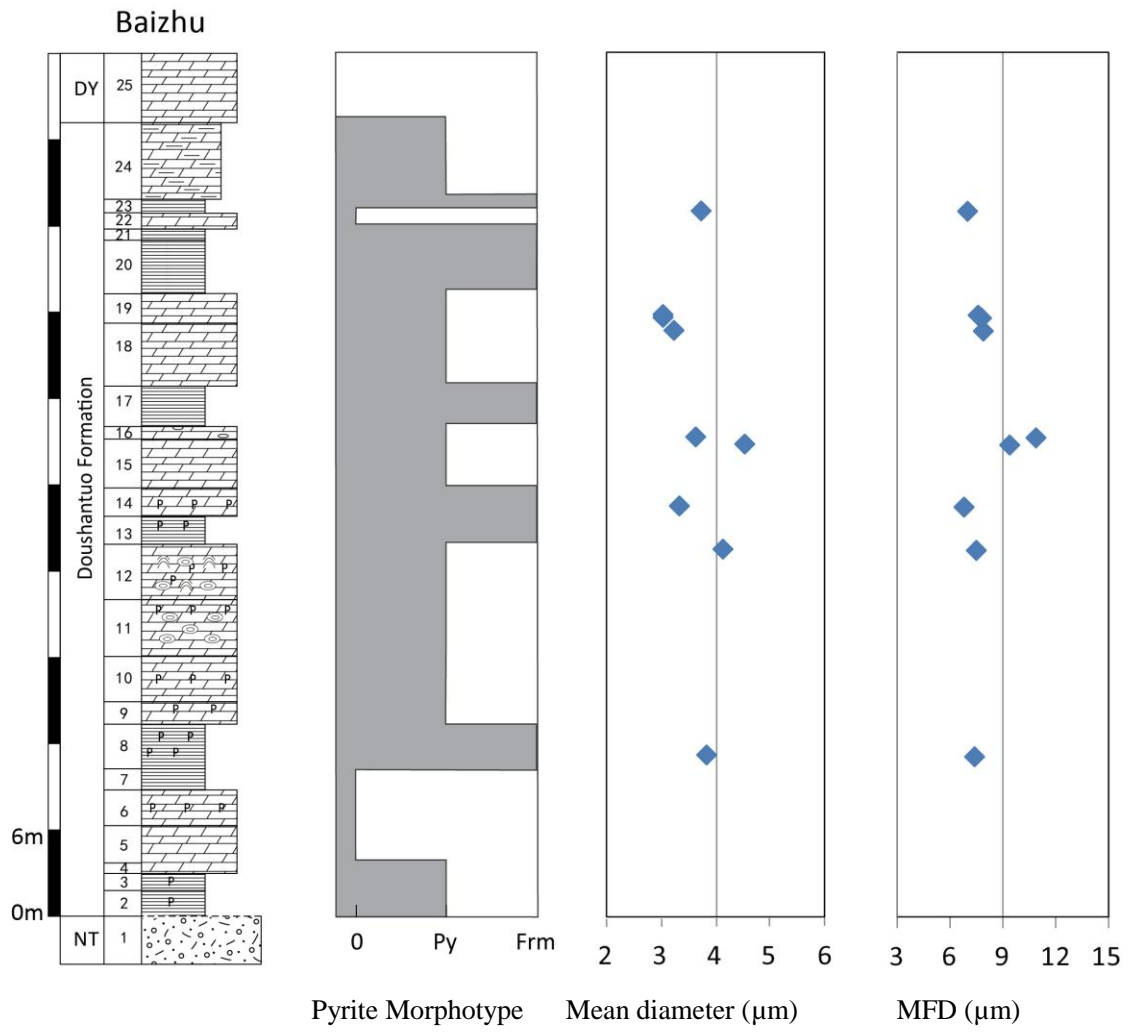












877

878

